Generation and modification of the mantle wedge and lithosphere beneath the West Bismarck Island Arc: melting, metasomatism and thermal history of peridotite xenoliths from Ritter Island.

*Author 1: Tollan, P.M.E., Institut für Geologie, Universtät Bern, 3012 Bern, Switzerland

Author 2: Dale, C.W., Department of Earth Sciences, Durham University, Durham DH1 3LE, United Kingdom

Author 3: Hermann, J., Institut für Geologie, Universtät Bern, 3012 Bern, Switzerland

Author 4: Davidson, J.P., Department of Earth Sciences, Durham University, Durham DH1 3LE, United Kingdom

Author 5: Arculus, R.J., Research School of Earth Sciences, The Australian National University, Canberra 2601, Australia

*Corresponding author, peter.tollan@geo.unibe.ch, +41 79 531 34 22

[1]**Previous addresses:** Research School of Earth Sciences, The Australian National University, Canberra 2601, Australia *and* Department of Earth Sciences, Durham University, Durham DH1 3LE, United Kingdom

[2]**Previous address:** Research School of Earth Sciences, The Australian National University, Canberra 2601, Australia

[4]**Deceased**

The Author 2017. Published by Oxford University Press. All rights reserved. For Permissions, please e-mail: journals.permissions@oup.com

Downloaded from https://academic.oup.com/petrology/article-abstract/doi/10.1093/petrology/egx062/4523818
by University of Durham user
on 07 November 2017

Abstract

Peridotite xenoliths dredged from the seafloor northwest of Ritter Island in the West Bismarck Island Arc offer a rare insight into the petrogenetic processes operating in the upper mantle wedge of an active oceanic subduction zone. Harzburgitic xenoliths and subordinate dunites and pyroxenites display significant textural and compositional variability between samples, which are interpreted as fragments of heterogeneous mantle that has experienced a complex petrogenetic history. Based on textures and *in situ* major and trace element analyses of olivine, orthopyroxene and clinopyroxene, five significant petrogenetic stages have been deduced. The first stage was a period of partial melting at temperatures >1100 ºC in a previously active arc (likely the now extinct Vitiaz West-Melanesian arc), indicated by the high Mg# and Cr#, low Al_2O_3 and very low concentrations of incompatible trace elements in residual phases and the absence of residual clinopyroxene. Modelling the concentrations of Y and Yb in orthopyroxene indicates depletion by high degrees (~30 %) of wet fractional melting of a depleted mantle source. This was followed by metasomatism also related to this previous period of subduction, resulting in refertilisation of the harzburgite residues with clinopyroxene and the formation of dunite and pyroxenite channels. Three populations of secondary clinopyroxene are identified based on their trace element compositions, with both LREE-depleted and (more unusually) sinusoidal REE patterns identified, indicating that a spectrum of fluid compositions was involved in the metasomatism. The third stage involved a period of cooling and chemical re-equilibration below the wet solidus, combined with decompression to shallow lithospheric mantle depths. Geothermometers with different closure temperatures reveal large temperature discrepancies, indicating mantle cooling was both unusually extensive (down to ~600 ºC), but also very slow

Downloaded from https://academic.oup.com/petrology/article-abstract/doi/10.1093/petrology/egx062/4523818
by University of Durham user
on 07 November 2017

(~20 ºC/My). The fourth stage marked the cessation of cooling and formation of the modern mantle wedge as part of the West Bismarck Island Arc. Silicate melts percolated through networks of veins and reacted with the residual mantle, generating a variety of new disequilibrium textures, most notably orthopyroxene-clinopyroxene-glass reaction patches. This was accompanied by increases in spinel Cr#, olivine trace element concentrations and higher mineral-mineral temperatures. These disequilibrium textures were preserved through the final stage of entrainment in the host basalt and rapid transport to the seafloor. The Ritter suite thus provides a remarkably detailed insight into the broad diversity of melt/fluid compositions and fluid-rock reaction processes in oceanic sub-arc mantle. Several of these features can be found both in other samples of sub-arc mantle and also cratonic mantle, demonstrating the ubiquity of such processes beneath modern arcs and also the potential genetic relationship between subduction zone processes and the formation of cratons. In this way, sub-arc xenoliths such as the Ritter suite, whilst presently under-sampled, can provide crucial insights for understanding the relationship between the mechanisms by which modern arc systems are generated and evolve, and the nature of the upper mantle once subduction processes have ceased.

Key words

peridotite xenolith, subduction zone, hydrous melting, sub-solidus cooling, diffusion, geothermometry, West Bismarck

Downloaded from https://academic.oup.com/petrology/article-abstract/doi/10.1093/petrology/egx062/4523818
by University of Durham user
on 07 November 2017

INTRODUCTION

The recycling of crust at subduction zones has been critical in forming the geochemical diversity of the silicate Earth. Upper arc crust is easily sampled from many active and extinct arcs and has provided important insights into the complex processes of magma generation and differentiation at subduction zones. A particular challenge, however, is to understand the nature of the mantle wedge beneath active arcs. Key areas of uncertainty are the composition and physical properties of the mantle wedge (Parkinson & Pearce, 1998; Arai & Ishimaru, 2008), the nature of the interaction and degree of chemical exchange between the mantle wedge and chemically distinct slab-derived fluids (Pirard & Hermann, 2015) and the conditions and mechanisms by which the mantle wedge melts (Till *et al.,* 2012). An improved knowledge of these areas is vital to understanding the dynamics of subduction zones, the role of the mantle wedge in moderating/buffering the composition of primary arc melts and the long-term balance of chemical fluxes between surface and mantle reservoirs (Plank & Langmuir, 1993).

The inversion of arc magma compositions to address these topics is complex because many compositional characteristics are ambiguous in origin or have been modified during magma ascent from the mantle to the surface. The most direct method, therefore, is to study fragments of the mantle wedge itself, exhumed at the surface as ultramafic xenoliths, since they offer the benefits of rapid exhumation and quenching from mantle depths, preserving textures and chemical signatures pertaining to the ambient mantle state (Pearson *et al.,* 2003). However, arc peridotite xenoliths are scarce compared to xenoliths recovered from other mantle domains, limiting our current level of knowledge. In addition, significant challenges remain in deciphering the chemical signatures of complex, multi-stage petrogenetic histories recorded by the whole-rock peridotites and their constituent phases. For example, it is commonly assumed that the

Downloaded from https://academic.oup.com/petrology/article-abstract/doi/10.1093/petrology/egx062/4523818
by University of Durham user
on 07 November 2017

concentrations and ratios of fluid-immobile elements such as the heavy rare earth elements (HREE) in residual pyroxenes reflect melting histories; however, recent studies have shown that these elements, whilst insensitive to metasomatism, may be redistributed and fractionated between residual phases as the mantle cools below its solidus (Witt-Eickschen & O'Neill, 2005; Lee *et al.,* 2007; Liang, 2014; McCoy-West *et al.,* 2015). This problem is exacerbated in particularly cold mantle fragments (including ophiolites) and therefore requires careful consideration of how different chemical species will respond to thermal perturbations before deducing the magnitude and nature of distinct, punctuated events such as melting or metasomatism. The few previous studies of arc peridotites have nevertheless revealed important insights into subduction zone processes. In particular, they have revealed greater detail on: (1) the composition and distribution of metasomatic fluids (Maury *et al.,* 1992; Kepezhinskas *et al.,* 1995; Franz *et al.,* 2002; Widom *et al.,* 2003; Ishimaru *et al.,* 2007; Vannuci *et al.,* 2007; Kamenov *et al.,* 2008; Bénard & Ionov, 2013); (2) mechanisms and timescales by which mantle-derived melts are transported through and interact with the surrounding ambient mantle (Arai *et al.,* 2004; Bryant *et al.,* 2007; Turner *et al.,* 2012; Tollan *et al.,* 2015); (3) the thermal and redox state of the mantle wedge (Brandon & Draper, 1996; Parkinson & Pearce, 1998; Parkinson *et al.,* 2003; Parkinson & Arculus, 1999; Ionov, 2010); (4) ancient melting events (Parkinson *et al.,* 1998).

In this contribution, we present and discuss the results of a detailed petrological and geochemical study of a lithologically diverse suite of peridotite xenoliths recovered from seamounts northwest of Ritter Island, West Bismarck island arc. The samples have textures established during ambient mantle and secondary reaction processes, often in a single hand specimen. By employing *in situ* analytical techniques we were able to identify specific

Downloaded from https://academic.oup.com/petrology/article-abstract/doi/10.1093/petrology/egx062/4523818
by University of Durham user
on 07 November 2017

compositions associated with the development of these distinct textures, and in doing so deduce a complex multi-stage history characterised by depletion and enrichment events in the sub-Ritter mantle.

GEOLOGICAL CONTEXT

The Bismarck Archipelago is situated north east of Papua New Guinea (Fig. 1). It is the result of a complex series of collisional and extensional events controlled principally by the oblique convergence of the Australian and Pacific plates at rates of around 20 cm/year, but fragmented into a number of micro-plates bounded variously by both active and inactive subduction systems (Woodhead *et al.,* 2010; Cunningham *et al.,* 2013). To the east, the oceanic Solomon Sea plate is subducting northwards beneath the South Bismarck plate, resulting in magmatism which has produced the New Britain island arc (or alternatively, East Bismarck island arc). To the west of New Britain, oblique collision between the South Bismarck and Australian plates initiated at around 3 to 3.7 Ma (Abbott *et al.,* 1994) and has led to the subduction-related magmatism of the West Bismarck island arc. Collision and magmatism began in the far west of the West Bismarck arc and gradually spread eastwards, such that collision at ~148° longitude, close to Ritter Island, began within the last million years, approximately coincidental with the opening of the Manus back-arc spreading centre to the north (Gill *et al.,* 1983). The composition of lavas erupted from the West Bismarck island arc are compositionally distinct from those of the New Britain arc to the east. This is thought to reflect different degrees of prior melting of their mantle sources, but both are fluxed by the same 'base' subduction component, perhaps introduced at the now extinct Manus/Kilinailau trench (Woodhead *et al.,* 1998; Woodhead *et al.,* 2010; Cunningham *et al.,* 2012; Fig. 1). West Bismarck arc lavas have subsequently incorporated additional sediment through crustal contamination during their ascent to the surface (Cunningham *et al.,* 2012) and

Downloaded from https://academic.oup.com/petrology/article-abstract/doi/10.1093/petrology/egx062/4523818
by University of Durham user
on 07 November 2017

span a broad range of compositions, from high-MgO basalts through to rhyolites. Distinct geochemical trends are observed along-arc such that volcanic rocks erupted in the eastern portion of the arc have the most primitive compositions. This is thought to reflect steadily decreasing degrees of partial melting westwards in response to arc-continent collision disrupting the typical subduction régime (Woodhead *et al.,* 2010).

Ritter is a small, crescent-shaped island located towards the most easterly extent of the West Bismarck Arc, approximately 25 km west of New Britain; its current shape and volume were established following the collapse of approximately 5 km^3 of the western flank of a pre-existing conical edifice on 13th March 1888 (Ward & Day, 2003). Several volcanic cones are emergent above the collapse debris flow to the northwest of Ritter, and are composed of pyroclasts of high-MgO (~15 wt %) olivine-clinopyroxene-plagioclase-phyric, low-Ti tholeiitic basalt (Tollan *et al.,* 2015). Ultramafic xenoliths (harzburgite, dunite and pyroxenite) encased in host basalt were dredged from a number of these volcanic cones during voyage SS06-2007 of Australia's Marine National Facility in July 2007, and are the first occurrences of mantle xenoliths recovered from volcanic centres in an active submarine oceanic arc system. The samples examined in this contribution were recovered from Cone 4 located at 5°28"N, 148°02"E and dredged from a water depth of ~1050 m (Fig. 1).

PETROGRAPHY

The Ritter sample suite is dominated by harzburgite, with subordinate dunite and pyroxenite (McAlpine, 2016; Bénard *et al*., 2016). A subset of this total sample suite was chosen for this study to represent the mineralogical and textural range present (Table 1). All samples collected are free of secondary alteration such as serpentinisation or weathering and hence fully retain both their mantle textures and the contact between the peridotite and host magma. The contact

Downloaded from https://academic.oup.com/petrology/article-abstract/doi/10.1093/petrology/egx062/4523818
by University of Durham user
on 07 November 2017

between the host magma and xenolith is clearly defined in all samples, irrespective of texture, and whilst there is evidence for populations of mantle xenocrysts in the host magma, there is no clear evidence for intrusion of the host magma into the xenolith or reaction at xenolith boundaries.

Protogranular harzburgite texture

Samples with protogranular textures are interpreted to reflect the ambient mantle, generated through sub-solidus equilibration following any previous melting or metasomatism (Fig. 2). Crystals of olivine and orthopyroxene are coarse (typically >2 mm in diameter) and have well-defined boundaries (Fig 2a, b). Olivine crystals typically have undulose extinction and sub-grain domains, whilst orthopyroxene has distinct fine exsolution lamellae. In a number of samples, olivine also has exsolved crystallographically-aligned plates of spinel. There is no obvious preferred crystal orientation or strain-induced elongation. Spinel usually occurs as individual coarse grains, or clusters of grains. More rarely, spinel clusters are arranged in linear trails. In thin-section, spinel has a brick-red core with a thin black rim which is shown to consist of fine contorted 'ropes' in backscattered scanning electron microscope (SEM) images. Rare clinopyroxene is much finer-grained (<0.5 mm in diameter), generally restricted to olivine-orthopyroxene triple boundaries and has grain boundaries that are often more irregular, indicating that clinopyroxene may not be a primary phase.

Harzburgite with reaction texture

Most of the samples show some evidence for secondary mineralogy, of which there are various types across the suite of samples (Fig. 2c, d, e, f; Fig. 3). The most common texture is patches or veins consisting mainly of fibrous orthopyroxene, which appears to form at the expense of

Downloaded from https://academic.oup.com/petrology/article-abstract/doi/10.1093/petrology/egx062/4523818
by University of Durham user
on 07 November 2017

olivine or, less commonly, residual orthopyroxene. Whereas orthopyroxene is the dominant phase present in these reaction patches, backscattered SEM images reveal minor amounts of much finer grained clinopyroxene and similarly small blebs of silicate glass, both of which are typically distributed interstitially (Fig. 3a, b, d, e). Small partially consumed grains of olivine can occasionally be observed as 'islands' within the reaction patches (Fig. 2f). In several samples, veins of secondary orthopyroxene crosscut larger residual olivine grains (Fig. 2d). The grain boundaries with residual phases are highly irregular with many embayments of secondary mineralisation at the rims of the residual phases (Fig. 2d, f; Fig. 3c). Spinel grains in samples containing secondary orthopyroxene or reaction patches have similar distribution and size to those associated with protogranular textures, but tend to lack the brick-red cores and instead have thin sieve-textured rims. Often the spinel contains inclusions of, or is associated with, thin trails of silicate glass. The presence and modal abundance of secondary orthopyroxene varies considerably between samples. In some samples these textures are completely absent, whereas in others they occur throughout the section. A few samples contain more sporadic occurrences of this reaction texture, indicating it is likely to be spatially highly heterogenous over larger volumes of mantle. One sample, 67-02D(4) shows a slightly different reaction texture, consisting of residual orthopyroxene partially reacting to form a mosaic of finely-distributed orthopyroxene (two populations: opx 1 and opx 2), clinopyroxene and glass (Fig. 3e). A less common type of vein consists solely of clinopyroxene. These veins appear to be better equilibrated with the surrounding peridotite, indicated by coarser grain sizes and more distinct grain boundaries. This type of vein is not limited to samples containing secondary orthopyroxene and there is no textural association between veins of secondary orthopyroxene and clinopyroxene. The absence of melt (glass) in the clinopyroxene veins is consistent with the higher degree of textural

Downloaded from https://academic.oup.com/petrology/article-abstract/doi/10.1093/petrology/egx062/4523818
by University of Durham user
on 07 November 2017

equilibration with the surrounding lithology and indicates that these veins probably predate the secondary orthopyroxene.

Dunite and pyroxenite

The dunites are texturally distinct compared with the harzburgites. For example, sample 67-02B(2), is distinguished by large pockets of very coarse, texturally homogenous spinel grains. Occasional fine fractures, which form a network around olivine grains, are surrounded by wisps of quenched melt. Dunite sample 67-02D(3) consists of a primary dunite with coarse olivine grains and occasional spinel grains, which is cross-cut by a secondary dunite vein composed of well-mixed, finer-grained olivine and spinel. There is no obvious reaction zone between the 'primary' dunite and the dunite vein and grain boundaries in both zones are well-defined. Sample 67-02A(3) has a porphyroclastic texture consisting of coarse 'relict' olivine and rarer orthopyroxene crystals and a fine-grained recrystallised matrix composed of neoblasts of olivine and clinopyroxene. This sample has been described in detail texturally and geochemically in a previous study (Tollan *et al.,* 2015) and represents a transition between ambient peridotite and clinopyroxene-bearing dunite. The two pyroxenites are dominated by orthopyroxene. 67-02A(1) approaches the orthopyroxenite end-member, with rare clinopyroxene grains, whereas 67-02B(6) contains more abundant clinopyroxene, which forms at the grain boundaries of orthopyroxene. In this sample, spinel is much more abundant, fine-grained and is texturally similar to spinel grains associated with reaction textures in the harzburgites. This sample contains a separate layer of almost pure clinopyroxene in which the grains have highly irregular grain boundaries and internal fractures. The boundary between the clinopyroxenite and orthopyroxenite layers is not well-defined, with evidence for mixing of populations of orthopyroxene and clinopyroxene.

Downloaded from https://academic.oup.com/petrology/article-abstract/doi/10.1093/petrology/egx062/4523818
by University of Durham user
on 07 November 2017

METHODS

Major elements

The major element composition of olivine, orthopyroxene, clinopyroxene and spinel were determined on a Cameca SX100 electron probe micro-analyser in wavelength-dispersive mode at the Research School of Earth Sciences, Australian National University. An operating voltage of 15 kV and current of 20 nA were used throughout, with a focused beam of 1 μm diameter. Counting times were 20 s for Mg, Al, Si, Fe and Cr, 30 s for Na, Ca and Mn and 60 s for Ti. In-house standards of San Carlos olivine, augite and chromite were measured at frequent intervals during the analytical sessions. Measurements were conducted typically on 3 grains per sample, with both cores and rims measured to establish compositional variability between and within grains. Additional major element data were collected using a JEOL-8200 at the Institut für Geologie, Universität Bern. Analytical conditions were the same except for counting times, which were 30 s for all elements.

Trace elements

In-situ trace element compositions were measured by laser ablation inductively coupled plasma mass spectrometry (LA-ICP-MS) at the Australian National University (ANU). The laser ablation system utilises a 193 nm ArF excimer laser with a custom-built 'HelEx' two-volume ablation cell which feeds into an Agilent 7700 quadrupole mass spectrometer. Ablation was conducted under an atmosphere of He and Ar, with 30 seconds of background measured prior to 40 seconds of ablation time. The laser was run at a frequency of 5 Hz, and a fluence of 3-4 J/cm^2 was used for all analyses. Olivine compositions (^{23}Na, ^{27}Al, ^{29}Si, ^{31}P, ^{43}Ca, ^{45}Sc, ^{47}Ti, ^{51}V, ^{53}Cr, ^{55}Mn, ^{59}Co, ^{60}Ni and ^{89}Y) were determined with a large 137 μm spot size except for crystal

Downloaded from https://academic.oup.com/petrology/article-abstract/doi/10.1093/petrology/egx062/4523818
by University of Durham user
on 07 November 2017

traverses which utilised an 81 μm spot size. Residual orthopyroxene compositions were determined for three adjacent spots. A single spot (81 μm) measured the same elements as in olivine, whereas the other two spots (137 μm) measured concentrations of ^{29}Si, ^{43}Ca, ^{47}Ti, ^{89}Y, ^{90}Zr, ^{93}Nb, ^{139}La, ^{140}Ce, ^{141}Pr, ^{143}Nd, ^{147}Sm, ^{153}Eu, ^{157}Gd, ^{159}Tb, ^{163}Dy, ^{165}Ho, ^{166}Er, ^{169}Tm, ^{192}Yb, ^{175}Lu and ^{178}Hf. The two neighbouring spots were checked for consistency and combined to give an average value. Data were reduced using the Iolite software package, with repeat measurements of either SRM NIST 610 or 612 glasses as primary calibration standards and ^{29}Si as the internal standard. Repeat analyses of standard natural glass BCR-2G were monitored for analytical consistency, with a relative standard deviation <8 % for all elements except Li and Ni (14 % and 28 % respectively). Data for NIST and BCR glasses were corrected against or compared with values reported in Jochum *et al.,* (2011) and the GeoReM online database respectively. For clinopyroxene, ^{88}Sr was added to the routine and the spot size reduced to 62 μm, due to the fine grain sizes. Measurements of secondary orthopyroxene and reaction patches were conducted in a later analytical session with a 105 μm spot size and with substantially improved sensitivity, permitting determination of ^{85}Rb, ^{138}Ba, ^{208}Pb, ^{232}Th, and ^{238}U concentrations.

RESULTS

Major Elements

Major element compositions of mineral phases are reported in Tables 2 and 3.

Olivine

Downloaded from https://academic.oup.com/petrology/article-abstract/doi/10.1093/petrology/egx062/4523818
by University of Durham user
on 07 November 2017

Coarse grained olivines in the protogranular harzburgites have a relatively restricted range of major element compositions (Fig 4a; Mg# (Mg/Mg+Fe) = 0.905-0.922, NiO = 0.37-0.52 wt %). The three dunites analysed contain olivine with a broader range of Mg# and NiO contents, although characterised particularly by the higher Mg# for a given NiO (Mg# = 0.914-0.947, NiO = 0.41-0.47 wt %). Dunite 67-02B(2) contains two populations of olivine: coarse refractory olivine with high Mg# 0.929-0.947 and a fine-grained (<100 μm) minor population associated with traces of melt with lower Mg# 0.914-0.919. The fine olivine also contains higher CaO and lower NiO compared to the coarse olivine. Aside from this exception, the compositional variability within each sample is very small, typically <1 %. There is no systematic difference between the major element composition of olivine from samples containing protogranular or reaction textures, although olivine porphyroclasts in sample 67-02A(3) show minor decreases in Mg# towards the crystal rims (Tollan et al. 2015).

Spinel

Spinel has a relatively large compositional range, with clear, albeit overlapping distinctions based on sample texture (Fig. 5). Spinel associated with protogranular textures has lower Cr# (Cr/Cr+Al = 0.495-0.614) and TiO_2 (<0.05-0.08 wt %), compared to spinel associated with glass-bearing reaction textures (Cr# 0.549-0.783 and TiO_2 0.08-0.37 wt %). Spinel from the pyroxenites is similar to spinel associated with protogranular textures, whereas spinel from the dunite is distinguished by its very high Cr# (up to 0.885).

Orthopyroxene

Coarse-grained protogranular orthopyroxene from the harzburgites has a similar compositional range to olivine and orthopyroxene from other arc peridotites (Fig. 4b), with Mg# ranging from

Downloaded from https://academic.oup.com/petrology/article-abstract/doi/10.1093/petrology/egx062/4523818
by University of Durham user
on 07 November 2017

0.910-0.925 and $Kd^{FeO/MgO}_{orthopyroxene/olivine}$ of 0.90-0.99. There is a good correlation between the forsterite content of olivine and orthopyroxene Mg#, in agreement with global melt depletion trends. Al_2O_3 and CaO contents are both very low (1.24-1.78 wt % and 0.40-1.12 wt % respectively). Orthopyroxene porphyroclasts from sample 67-02A(3) have uniquely low Al_2O_3 (0.89 wt %) and higher CaO (1.23 wt %). As with olivine, there is no clear distinction between orthopyroxene from samples with contrasting textures. Orthopyroxene in the pyroxenites is similar in composition to that from the harzburgites, except for slightly lower Al_2O_3 (1.15 wt %), whereas orthopyroxene in the orthopyroxenite has a relatively low Mg# (0.900). Orthopyroxenes in reaction patches (Table 3) have similar compositions to the residual orthopyroxene from the same sample. Sample 67-02D(4) contains two populations of orthopyroxene, identified visually by their different contrast in backscattered electron imaging (Fig. 3e). Orthopyroxene 1 has uniquely higher Mg# (0.96), lower MnO and CaO and higher Cr_2O_3 and Na_2O, whereas orthopyroxene 2 has a composition similar to the other reaction and residual orthopyroxenes.

Clinopyroxene

Clinopyroxene in the harzburgite is distinctively low in Al_2O_3 (1.15-2.41 wt %) and Na_2O (0.01-0.23 wt %) compared with clinopyroxene in abyssal peridotites (Fig. 4c), coupled with high CaO (typically 22.15-24.10 wt %) and high Mg# (typically 0.943-0.954). All of these features are characteristic of compositions previously reported for clinopyroxene in arc peridotites (Fig 4c, d). There is a negative correlation between Na_2O and both Mg# and CaO (Fig. 4d). More compositional variation is observed in clinopyroxene than for other phases. This is most apparent for two samples, 67-02B(5) and 67-02D(7). Three clinopyroxene analyses in the former show significant variation in Mg# (0.908-0.925), which correlates negatively with TiO_2. Sample 67-02D(7) contains two populations of clinopyroxene (randomly dispersed and vein-concentrated),

Downloaded from https://academic.oup.com/petrology/article-abstract/doi/10.1093/petrology/egx062/4523818
by University of Durham user
on 07 November 2017

the former with higher Mg# and CaO (0.934 and 22.69 wt % respectively) compared to lower values of 0.859 and 21.43 wt % in the vein population. Significantly, there is no compositional difference between clinopyroxene comprising the veins in protogranular sample 67-02E(1) and any of the other clinopyroxene populations, other than the exceptions described above. There is no clear relationship between the Mg# of clinopyroxene and the forsterite content of olivine. $Kd^{FeO/MgO}_{clinopyroxene/olivine}$ values deviate significantly from unity (0.52-0.83, with the exception of 67-02B(5) which has a mean value of 1.01), most likely due to the greater compatibility of Fe^{3+} in clinopyroxene. Clinopyroxene in the pyroxenites is similar to that in the harzburgites, but with slightly higher FeO. Clinopyroxene in dunite 67-02D(3) has lower Al_2O_3 and higher Mg# and CaO than clinopyroxene in harzburgite, Clinopyroxene neoblasts in the transitional dunite sample 67-02A(3) are also compositionally distinct, with lower Al_2O_3 (0.55 wt %) and CaO (20.37 wt %). The very fine-grained interstitial clinopyroxene in the reaction patches (Table 3) is distinguished by lower Mg# (0.90-0.91) and CaO (~18.5 wt %).

Trace Elements

Orthopyroxene

The trace element compositions of coarse-grained orthopyroxene are reported in Table 4. Orthopyroxene has very depleted trace element compositions compared to the limited data available from abyssal samples (Hellebrand *et al.,* 2005; Seyler *et al.,* 2011). Data for orthopyroxene from other arc (or purported arc) peridotites are even scarcer, with the Ritter samples showing similar levels of depletion to the few published examples (e.g. Parkinson *et al.* 2003; Ionov, 2010; Pirard *et al.,* 2013). On primitive mantle-normalised rare earth element (REE) plots (Fig. 6), orthopyroxene typically has slightly spoon-shaped patterns, with steeply inclined heavy (H)REE, relatively flat medium (M)REE and flat to slightly enriched light

Downloaded from https://academic.oup.com/petrology/article-abstract/doi/10.1093/petrology/egx062/4523818
by University of Durham user
on 07 November 2017

(L)REE. Multiple orthopyroxene grains from the same sample have similar concentrations of all REE, although a few samples contain orthopyroxene with increasingly dispersed REE concentrations from the HREE through to the LREE (Fig. 6).

Orthopyroxenes in the different samples share similar REE concentrations and patterns, irrespective of the dominant texture. HREE concentrations overlap in a tight group, whereas LREE concentrations typically show much greater variability, beyond analytical uncertainty. On extended trace element plots (Fig. 6), there is a positive Ti anomaly for orthopyroxene from all samples, however this anomaly mainly reflects the greater compatibility of Ti in orthopyroxene relative to other trace elements and disappears once Ti is repositioned accordingly between Er and Yb (McDade *et al.,* 2003). Orthopyroxenes from some samples also have positive Hf and Zr anomalies, which can be explained similarly. Very strong positive Nb anomalies are consistently observed, whereas concentrations of Nb do not correlate with any other measured trace element in orthopyroxene. Orthopyroxenes in the pyroxenites (not shown) have nearly identical normalised trace element patterns to those in harzburgite, but tend to be slightly more enriched for most elements, with LREE and Nb the exceptions (Nb anomalies are always weaker).

Secondary orthopyroxene and reaction patches

Whereas reaction patches are composed dominantly of orthopyroxene, the frequent occurrence of interstitial glass and clinopyroxene in all but one sample made it impossible to analyse the separate phases. Individual laser points therefore encompass varying proportions of all three phases; based on the low CaO concentrations in each analysis (< 2 wt %), however, it is clear that orthopyroxene is always the dominant contributor to the bulk analysed composition. Reaction patches from both 67-02A(5) and 67-02D(4) reveal substantial increases in

Downloaded from https://academic.oup.com/petrology/article-abstract/doi/10.1093/petrology/egx062/4523818
by University of Durham user
on 07 November 2017

incompatible trace element concentration over residual orthopyroxene from the same samples (Fig 7a-c). Less incompatible REE show smaller degrees of enrichment compared to more incompatible REE, a pattern which generally applies to the other trace elements. Elements which are notable exceptions are Ti, Zr and Nb, all of which show less enrichment in reaction patches compared to elements of similar compatability such as Eu, Sr and Ce (Fig 7d-f). For Ti this results in the reversal of the positive Ti anomalies observed in residual orthopyroxene. Sample 67-02B(3) contains substantially less interstitial glass and no clinopyroxene, confirmed by the very low CaO concentrations (typically <0.5 wt %). The general pattern of enrichment is similar to reaction patches from other samples, although to generally lower degrees, particularly for the REE. The salient features from the reaction patches discussed above are all present, particularly very strong positive Sr anomalies in the secondary orthopyroxene, compared to no or negative anomalies in the residual orthopyroxene.

Clinopyroxene

Due to the scarcity and fine-grained nature of clinopyroxene in the Ritter suite, analyses were restricted to six harzburgites (with dominantly protogranular textures) and the two pyroxenites, where grains could be clearly distinguished and were optically inclusion-free (Table 5). Clinopyroxene has much greater diversity in trace element composition than orthopyroxene, with three distinct primitive-mantle normalised REE patterns (Fig. 8). Type I clinopyroxene occurs in three harzburgite samples and the two pyroxenites. They display similar patterns with relatively flat HREE, gently downward-dipping LREE and La_N/Lu_N of 0.2-0.6. Two harzburgites contain type II clinopyroxenes which display more complex sinusoidal patterns showing general enrichment in LREE over HREE, peaks at Nd and Lu and a minimum at Ho. The anomalously low-Mg# type III vein clinopyroxene from harzburgite 67-02D(7) are overall more enriched than

Downloaded from https://academic.oup.com/petrology/article-abstract/doi/10.1093/petrology/egx062/4523818
by University of Durham user
on 07 November 2017

any other clinopyroxene measured, with normalised concentrations increasing from HREE through MREE before relatively steeply downward-dipping LREE. Small variations between individual crystals within a sample are also apparent, generally no more than by a factor of 2-3. Type I clinopyroxene from 67-02E(1) has distinct negative Eu anomalies, despite having similar overall REE patterns to other type I clinopyroxenes. On extended trace element plots, additional diversity is observed (Fig. 8). All clinopyroxene types display positive Sr anomalies and slightly to strongly negative Ti anomalies. Zirconium and Hf anomalies vary from strongly negative to absent whereas all clinopyroxene has very strong negative Nb anomalies. Type II clinopyroxenes tend to have more extreme trace element anomalies compared to type I and type III clinopyroxene, particularly the magnitude of the Ti anomaly, with Ti/Eu ratios as low as 200 compared with typical values of >1000 for type I and type III clinopyroxene.

Olivine

Trace element data for olivine are summarised in Table 6 and Fig. 9. Unlike orthopyroxene and clinopyroxene, there is a distinction in trace element composition according to sample texture. Olivine associated with protogranular textures contain very low concentrations of most elements compared to global mantle olivine data (Fig. 9, Table 6). Concentrations of Al, Cr and V are particularly low (Fig 9; 1.06-9.82 ppm, 3.99-28.60 ppm and 0.234-1.020 ppm respectively). However, during analysis, significant intensity spikes for these elements were noted, indicating partial ablation of the spinel exsolutions commonly observed during sample preparation (Supplementary Data Fig. 1). Sample 67-02E(1), which has higher concentrations of Ti in spinel, clinopyroxene and orthopyroxene, also has higher concentrations of Ti in olivine, suggesting all four phases are in equilibrium. There is no clear relationship between the concentrations of different trace elements in olivine, either within any given sample or on a suite-wide basis.

Downloaded from https://academic.oup.com/petrology/article-abstract/doi/10.1093/petrology/egx062/4523818
by University of Durham user
on 07 November 2017

Olivines from samples with glass-bearing reaction patches display more variation in trace element concentrations (Fig. 9, Table 6). These variations occur both on a sample-wide scale and between olivine in individual samples, indicating a high degree of trace element disequilibrium. The concentrations overlap with the narrow compositional space defined by olivine associated with protogranular textures (Fig. 9), but extend to concentrations over an order of magnitude greater for some elements. Elements which show no clear distinction between olivine from the two sample groups are P and Co. Laser ablation of individual olivine grains showed little or no evidence for spinel exsolution compared to olivine associated with protogranular textures.

Olivines from two of the dunite samples are very similar in composition to olivine associated with protogranular textures, with generally very low concentrations of all incompatible trace elements. In particular, olivine from 67-02B(2) is exceptionally depleted in V, containing as little as 0.03 ppm. There is no difference in the trace element composition of fine-grained olivine from the fine-grained dunite vein compared to coarse dunitic olivine in sample 67-02D(3). A sample intermediate between harzburgite and clinopyroxene-bearing dunite (67-02A(3)), shows olivine trace element compositional variation which encompasses almost the entire range for olivine in all other samples combined. This was discussed at length by Tollan *et al.* (2015), who interpreted this chemical variation to reflect diffusional re-equilibration during reaction with primitive basalts in the upper mantle wedge, shortly before entrainment and eruption.

DISCUSSION

The textural and compositional data preserved in the Ritter samples can be interrogated to reveal a detailed geological history, providing new perspectives on both the nature of ambient upper

Downloaded from https://academic.oup.com/petrology/article-abstract/doi/10.1093/petrology/egx062/4523818
by University of Durham user
on 07 November 2017

mantle underlying modern oceanic island arcs and, more broadly, the role that subduction played in the evolution of the Bismarck Archipelago. Five clear petrogenetic stages can be identified in the data presented (Fig. 10): (1) hydrous partial melting in a palaeo-island arc system; (2) clinopyroxene metasomatism; (3) sub-solidus cooling; (4) metasomatism beneath the currently-active West Bismarck island arc; (5) Exhumation. The following discussion begins with the results of thermometry calculations before presenting the textural and chemical evidence for each stage in the samples' history, starting with the earliest and ending with the most recent, before placing the results in the context of our current understanding of arc magmatism in the Bismarck Archipelago.

Geothermometry

Establishing the equilibration temperature of peridotite xenoliths provides essential information into the thermal structure of the upper mantle, the metasomatic and exhumation history of the sampled lithology, and is a prerequisite for further interpretation of the concentrations of chemical components which have temperature-sensitive partitioning behaviour in peridotite assemblages. Calculations of temperature typically utilise calibrations involving coexisting mineral pairs such as olivine-spinel and orthopyroxene-clinopyroxene, and assume chemical equilibrium of the components involved in the respective exchange reactions. The most popular calibrations involve exchange of major or minor elements, such as Fe, Mg and Ca (e.g. Wall & O'Neill, 1987; Brey & Köhler, 1990). The partitioning of many other minor and trace elements between respective phases in peridotites are also temperature-sensitive. A number of recent studies have attempted to calibrate the inter-mineral partitioning of these elements as alternative

Downloaded from https://academic.oup.com/petrology/article-abstract/doi/10.1093/petrology/egx062/4523818
by University of Durham user
on 07 November 2017

thermometers (Witt-Eickschen & O'Neill, 2005; Liang & Sun, 2013; Coogan *et al.,* 2014). Such studies have a number of benefits. Firstly, expanding the range of thermometric calibrations to elements with different diffusivities (and thus closure temperatures) opens up possibilities of constraining more detailed thermal histories. Secondly, calculating apparent temperatures from a wide range of trace elements permits more detailed insights into metasomatic processes which may have additionally influenced the distribution of trace elements in a sample. Finally, determining the temperature-dependent partitioning behaviour of trace elements facilitates corrections for element exchange during sub-solidus cooling, allowing reconstruction of the trace element composition of residual phases at conditions appropriate for modelling of partial melting and other high-temperature events (Fig. 11).

To explore in detail the temperature history of the Ritter samples, temperatures were calculated from a range of thermometers which rely upon the exchange of components with different diffusivities and therefore closure temperatures (Dodson, 1973). The slowest diffusing components which have been calibrated as a thermometer are the exchange of REE between two pyroxenes (Van Orman *et al.,* 2001; Witt-Eickschen & O'Neill, 2005; Cherniak & Liang, 2007; Lee *et al.,* 2007; Liang & Sun, 2013), whereas the thermometer subject to the most rapid re-equilibration involves Fe-Mg exchange between olivine and spinel (Wall & O'Neill, 1987; Dohmen & Chakraborty, 2007). Intermediate rates of re-equilibration involve major component (Fe-Mg, Ca) exchange between two pyroxenes (Brey & Kohler, 1990; Zhang *et al.,* 2010; Müller *et al.,* 2013). Finally, thermometers based on Al exchange between olivine and spinel are thought to better record peak temperatures (De Hoog *et al.,* 2010; Coogan *et al.,* 2014) due to slow diffusion of Al in olivine, although this assumption is based on a relatively scant amount of diffusion data (Spandler & O'Neill, 2010).

Downloaded from https://academic.oup.com/petrology/article-abstract/doi/10.1093/petrology/egx062/4523818
by University of Durham user
on 07 November 2017

One of the main advantages of traditional thermometers utilising the exchange of major and minor components (O'Neill & Wall, 1987; Brey & Köhler, 1990), is that the necessary data can be readily acquired by EPMA as opposed to LA-ICP-MS, which is required for thermometers based on trace element exchange. Since EPMA employs typically far superior imaging methods and smaller spot sizes, it is considerably easier to obtain data on samples with only trace amounts of key phases, such as clinopyroxene in the Ritter harzburgites which display reaction textures. For this reason, we were able to collect considerably more traditional thermometry data for Ritter samples than for trace element-based thermometers, as can be seen by comparing Fig. 12a and 12b. Fig. 12a displays temperatures calculated from olivine-orthopyroxene (Wall & O'Neill, 1987) and clinopyroxene-orthopyroxene (Brey & Köhler, 1990) equilibria. There is a clear trend between samples displaying protogranular and reaction textures, with the former forming a tight, overlapping cluster at both low two-pyroxene and olivine-spinel temperatures (790-860 °C and 660-760 °C respectively). Samples displaying reaction textures then follow a trajectory away from this to much higher tempeartures, with good correlation between the two calibrations (with the exception of one sample). Irrespective of texture, though, there is a consistent offset between the two methods, with olivine-spinel temperatures 50-150 °C lower than two-pyroxene temperatures.

For the reasons explained above, trace element-based thermometers could only be applied to samples where coarse clinopyroxene was present, as fine-grained material was impossible to identify using the imaging optics of the laser ablation instrument. This restricted the available samples only to those five which were dominated by protogranular textures.These five samples display a very broad range of temperatures with differences of 240-370 °C between the highest and lowest temperature estimates from different methods for individual samples (Table 7, Fig.

Downloaded from https://academic.oup.com/petrology/article-abstract/doi/10.1093/petrology/egx062/4523818
by University of Durham user
on 07 November 2017

12). The highest temperatures were calculated with the two pyroxene REE exchange thermometer of Liang & Sun (2013) which employs an inversion procedure of measured partition coefficients for the full suite of REE (+ Y). This not only produces a robust temperature estimate but also provides a simple method of determining the degree of equilibrium. Application to the Ritter samples shows that the elements Lu through to Sm for two pyroxene pairs all fall on the same regression line, indicating they reflect equilibrium partitioning at the same temperatures (820-1000 ºC). The remaining LREE deviate away from this equilibrium slightly, which could be attributed to a metasomatic event disturbing LREE concentrations or to the slower diffusion rates of LREE (Van Orman *et al.,* 2001). To examine the possibility of the latter, temperatures were calculated just from the exchange of Ce, resulting in values of 1010-1220 ºC, ~200 ºC higher than temperatures calculated from MREE and HREE. Given that these temperatures are well within the range of realistic values for the upper mantle, it is possible that LREE concentrations in pyroxenes may still be at or close to equilibrium, but at higher temperatures than recorded by the exchange of other components.

The lowest temperatures for these five samples were calculated from Fe-Mg and Al exchange between olivine and spinel (660-760 ºC and 650-740 ºC respectively). Whereas the much lower Fe-Mg olivine-spinel exchange temperatures are easily reconciled due to the much faster rates of Fe-Mg diffusion in olivine and spinel compared to REE diffusion in pyroxenes (Müller *et al.,* 2013), the low Al exchange temperatures apparently contradict the current experimental diffusion data (Spandler & O'Neill, 2010). A plausible solution to this discrepancy is the influence of spinel exsolutions within olivine grains associated with the protogranular texture which strongly partition Al, Cr and V into their structure. The distribution of this exsolved spinel significantly reduces the diffusion distance required for these elements to

Downloaded from https://academic.oup.com/petrology/article-abstract/doi/10.1093/petrology/egx062/4523818
by University of Durham user
on 07 November 2017

achieve equilibrium and hence may have facilitated equilibration to such low temperatures. Alternatively, this thermometry result may indeed indicate that Al diffuses through olivine significantly faster than previously recognised, which would jeopardise studies employing these thermometers to determine peak crystallisation temperatures (e.g. Heinonen *et al.,* 2015). The two pyroxene thermometers of Brey & Köhler (1990) both produce temperatures intermediate between the olivine-spinel and two pyroxene REE thermometers (Table 7, Fig. 9), which is again consistent with the rate of diffusion for the major components involved in the exchange reactions. Temperatures calculated from the formulation involving both pyroxene compositions are 790-860 ºC whereas temperatures calculated just from the orthopyroxene record slightly higher and less varied temperatures (890-910 ºC).

To investigate the influence of temperature on the inter-mineral distribution of other elements, olivine/pyroxene partition coefficients for Al, Cr, V, Sc and Y were calculated for the Ritter samples displaying homogeneous mineral compositions and plotted against temperature calculated from olivine-spinel Fe-Mg exchange (Fig. 13). Agreement or disagreement with the results of this well-established thermometer thus give an indication of the temperature sensitivity of partitioning of other elements between different phases, and the rate at which such element exchange can maintain equilibrium during sub-solidus cooling. Literature data for well-equilibrated peridotites from the studies of Witt-Eickschen & O'Neill (2005), Witt-Eickschen *et al.,* (2009) and De Hoog *et al.,* (2010), along with the high temperature experiments of Davis *et al.,* (2013) define good trends for partitioning of these elements as a function of temperature. Regression lines based on the relationship $D_{Pyroxene/olivine} = \left(\frac{T}{a}\right)^b$ (where 'D' is the partition coefficient between pyroxene and olivine, 'T' is temperature in degrees Celsius and 'a' and 'b' are constants) were calculated from this literature data. The partitioning of V, Cr and Y between

Downloaded from https://academic.oup.com/petrology/article-abstract/doi/10.1093/petrology/egx062/4523818
by University of Durham user
on 07 November 2017

clinopyroxene and olivine is broadly consistent with the regressions and temperatures calculated from olivine-spinel equilibria (Fig. 13a, b; Supplementary Data). This is a strong indication that despite falling considerably outside the calibration range of the thermometers used, the partitioning behaviour of these elements is still, at least to an approximation, consistent when such calibrations are extrapolated to more extreme conditions. Scandium, however, falls completely off the regression line, indicating disequilibrium at the calculated temperatures (Supplementary Data Fig. 3). The partitioning of Al, Sc, Cr, V and Y between orthopyroxene and olivine is also consistent with low temperature equilibration for these elements (Fig. 13e, f). However, these elements tend to fall off the regression slightly, in particular Cr (Fig. 13e) and Y, indicative of slightly lower equilibration temperatures than olivine-spinel equilibria. Such low temperatures, despite the slow diffusion rate for these elements in pyroxene, can be explained by the minor's rule (Liang, 2014) whereby the time required for diffusive equilibration is dictated by the mineral which contains the lowest concentration of a particular element. In a peridotite, particularly highly refractory varieties, olivine contains substantially lower concentrations of most incompatible trace elements than the combination of orthopyroxene and clinopyroxene. Hence a much smaller element flux is required to shift the bulk composition of olivine relative to the pyroxenes. In contrast, partition coefficients between orthopyroxene and clinopyroxene clearly do not reflect equilibrium at the calculated olivine-spinel temperatures, instead plotting at D values consistent with much higher temperatures of equilibration (Fig. 13c,d), as supported by independent orthopyroxene-clinopyroxene thermometry results (Table 7; Fig. 12; Fig. 14).

Conditions and environment of melting

Downloaded from https://academic.oup.com/petrology/article-abstract/doi/10.1093/petrology/egx062/4523818
by University of Durham user
on 07 November 2017

Previous studies of arc peridotite xenoliths and exhumed sections of fore-arc mantle have reached various conclusions concerning melting histories, ranging from melting occurring entirely in an anhydrous, spreading centre setting followed by modification by arc melts or fluids (Parkinson & Pearce, 1998; Pearce *et al.,* 2000; McInnes *et al.,* 2001; Jean *et al.,* 2010; Batanova *et al.,* 2011) to melting occurring in a hydrous, mantle wedge environment, preceded by varying degrees of melt-generation at an oceanic or back-arc spreading centre (Bizimis *et al.,* 2000; Franz *et al.,* 2002; Ishimaru *et al.,* 2007; Ionov, 2010; Pirard *et al.,* 2013). In a number of cases, complex post-melting metasomatism and ambiguity in interpreting chemical tracers of tectonic setting prevent a clear discrimination between plausible melting scenarios (Parkinson & Arculus, 2003; Vannucci *et al.,* 2007). Nevertheless, it is clear that global occurrences of 'arc mantle' do not share common petrogenetic histories and may represent several stages of melting in a variety of environments. This is in contrast to abyssal peridotites, which are generally regarded as the residues of polybaric, near-fractional melting event (Johnson, 1990; Hellebrand *et al.,* 2002; Brunelli *et al.,* 2006; Seyler *et al.,* 2011).

Studies of mafic and intermediate magmas erupted along the West Bismarck and New Britain (East Bismarck) Island Arcs have identified complex petrogenetic histories involving melting as part of the present-day arc systems, but also evidence for a previous episode of subduction unrelated to the active arcs (Woodhead *et al.,* 1998; Woodhead *et al.,* 2010, Cunningham *et al.,* 2012). Whilst the very low equilibration temperatures of the Ritter peridotites displaying protogranular textures preclude them from having experienced melting as part of the active arc, they may still preserve a memory of previous melting environments and at a resolution not possible to attain with studies of magmas erupted from the extant arc. The most simple and commonly used approach in addressing this is to compare the olivine and spinel

Downloaded from https://academic.oup.com/petrology/article-abstract/doi/10.1093/petrology/egx062/4523818
by University of Durham user
on 07 November 2017

major element compositions to the olivine-spinel mantle array (OSMA) of Arai *et al.,* (1994), which seems to discriminate between peridotites formed through partial melting in a variety of tectonic environments. One assumption with such an approach is that the major element compositions of olivine and spinel are not affected by subsequent processes, which may variably affect different mantle domains. Sub-solidus cooling, for example, is a ubiquitous process that can vary considerably in both rate and magnitude. Spinel Cr# has been shown to be moderately susceptible to this process, with a potential to decrease by up to 10 % over the temperature range 1300-800 °C (Voigt & von der Handt, 2011). However, unless a given mantle sample can be shown to have experienced a particularly unusual rate or magnitude of cooling, the relative change to spinel composition between any given sample should be much smaller than this. Whilst spinel Cr# is relatively insensitive to cooling, it may be disturbed significantly by melt-rock reaction, a process which can similarly affect olivine. This is particularly true for harzburgitic mantle, where melt-rock interactions can result in significantly higher values of both spinel Cr# and olivine Mg#, distorting or irradicating the signature of partial melting (Parkinson *et al.,* 2003; Suhr *et al.,* 2003; Morgan *et al.,* 2008; Batanova *et al.,* 2011; Morishita *et al.,* 2011). Taking samples only bearing the protogranular texture, which have not obviously experienced melt-rock reaction, olivine-spinel compositions all plot within the arc field, although some are not distinguishable from the overlapping abyssal peridotite field (Fig.5). Given the unusually large magnitude of cooling and the harzburgitic lithologies, it is possible that the values were even more refractory at the conditions of partial melting, making the distinction even clearer (Voigt & von der Handt, 2011). This superficially supports an arc origin for the Ritter mantle. However the predominance of secondary textures and lithologies in the sample suite, and the possibility of chemical exchange between modally reacted and un-reacted mantle, requires

Downloaded from https://academic.oup.com/petrology/article-abstract/doi/10.1093/petrology/egx062/4523818
by University of Durham user
on 07 November 2017

confirmation by other indicators of provenance, which are less susceptible to the secondary processes. Thus, an alternative chemical distinction is discussed below.

Whereas experimental studies of melting reactions and trace element partitioning in hydrous systems are relatively scarce, so far such studies have shown some important differences from the anhydrous equivalents. Firstly, the proportion of clinopyroxene entering the melt is lower under hydrous conditions (Gaetani & Grove, 1998) and secondly, the compatibility of trace elements in clinopyroxene is lower under hydrous conditions (McDade *et al.,* 2003). The combined effect, on a given starting composition and assuming closed-system fractional melting, is that at the point of clinopyroxene exhaustion during hydrous melting, whole-rock and mineral compositions will be more depleted in incompatible trace elements than is the case for anhydrous melting. This distinction has previously been noted and used by Bizimis *et al.,* (2000) and Jean *et al.,* (2010) to demonstrate a hydrous, arc origin for various ophiolites. We adopt a similar approach to these previous studies. However, instead of utilising clinopyroxene compositions we use orthopyroxene. This is because the distribution of clinopyroxene in veins and at crystal triple junctions, and the occurrence of sinusoidal clinopyroxene REE patterns indicates that clinopyroxene is either not a primary phase or has been metasomatically overprinted. Therefore, comparison between the compositions of orthopyroxene, which is almost universally found as a residual phase, is more appropriate. In addition, there is now a substantial amount of data for orthopyroxene trace element compositions from abyssal peridotites with which to compare data from arc peridotites (Hellebrand *et al.,* 2005; Warren *et al.,* 2009; Brunelli & Seyler, 2010; Seyler *et al.,* 2011). In order to determine peridotite melting histories it must be clearly demonstrated that the chosen melting proxy has remained undisturbed during post-melting modification by metasomatic fluids. In the Ritter samples, the very low concentrations and

Downloaded from https://academic.oup.com/petrology/article-abstract/doi/10.1093/petrology/egx062/4523818
by University of Durham user
on 07 November 2017

homogeneous distribution of mildly incompatible trace elements (HREE, Y, Sc, Ti, V etc.) in orthopyroxene cores, from both the same sample and from texturally distinct samples, support this assertion. Moreover, the primary, equilibrated textures of the orthopyroxene crystals analysed is strong evidence for minimal metasomatism and thus these elements can be used to unravel melting histories. An additional requirement is that there was minimal chemical re-equilibration between phases during cooling below the melting temperature, or that this is appropriately corrected for. In the case of Y and Yb in orthopyroxene, we found the impact of cooling to be negligible in this regard; this will be discussed in further detail in a later section.

The mantle melting model consisted of simple, isobaric fractional melting. Batch melting was also considered, however the magnitude of depletion recorded by the Ritter samples means that batch melting scenarios are insufficient to explain the spread of data (e.g. Johnson *et al.,* 1990). In order to make the comparisons between hydrous and anhydrous melting as meaningful as possible, partition coefficients for clinopyroxene and orthopyroxene were used from the same researchers or laboratories; McDade *et al.,* (2003b) for anhydrous values at 1.5 GPa and 1315 °C and McDade *et al.,* (2003a) for hydrous values at 1.3 GPa and 1245 °C. Olivine partition coefficients are from Mallmann & O'Neill (2013) and are anhydrous only, although olivine D values and concentrations are so low they make very little difference to the model outcome. The anhydrous melting reaction is from Baker & Stolper (1994) and the hydrous melting reaction from Gaetani & Grove (1998). The melting model utilises equation (32) from Zou (1998), which is for non-modal 'dynamic' melting (essentially fractional melting with an added porosity term to allow modelling of the effect of a small proportion of trapped melt). This equation allows calculation of the concentration of a trace element in the residue for a given degree of partial melting. Following this, the concentration of the element in residual orthopyroxene was

Downloaded from https://academic.oup.com/petrology/article-abstract/doi/10.1093/petrology/egx062/4523818
by University of Durham user
on 07 November 2017

calculated (see Appendix for a complete description of the equations used). The elements Y and Yb were chosen for the model comparisons since they are both relatively easily measured in orthopyroxene whilst displaying slightly different compatibilities (Y is chemically analogous to Ho but is easier to measure since it is present at higher concentrations). The results of the models are shown in Fig. 11. The data for abyssal peridotites are reproduced well by the anhydrous melting model up to the point of clinopyroxene exhaustion and, whilst the melting model employed here is a simplification of the actual melting process at spreading centres, it clearly shows that the exhaustion of clinopyroxene is a limiting factor to melt productivity. The data for orthopyroxene from Ritter peridotites is considerably more depleted than any of the abyssal samples or the anhydrous melting model, requiring the melting regime to be hydrous. In fact, even though the hydrous melting model predicts substantially more depleted orthopyroxene compositions, the majority of Ritter samples are more depleted still. To model these more depleted compositions the hydrous harzburgite melting reaction from Parman & Grove (2004) was used. An additional 4% of harzburgite melting is required to fully encompass all Ritter compositions, meaning the total amount of hydrous melting predicted by our models is ~26-33%. A limitation of such extreme melting models is the use of fixed partition coefficients for the entirety of melting. In reality, as melting progresses the major element compositions of the constituent phases will also change. In particular, the Al content of both pyroxenes will decrease, resulting in progressively lower partition coefficients for many trace elements, such as the REE (Blundy & Wood, 1994; Liang *et al.,* 2013). Because of this, our model results should be considered maximum values. Such contrasting degrees and styles of melting between the Ritter peridotites and abyssal peridotites do not necessarily rule out a period of spreading centre melting as part of the petrogenesis of sub-arc mantle beneath the West Bismarck island arc. It

Downloaded from https://academic.oup.com/petrology/article-abstract/doi/10.1093/petrology/egx062/4523818
by University of Durham user
on 07 November 2017

does, however, require a much more complex melting history, likely involving a protracted period within a subduction zone setting.

Clinopyroxene-metasomatism

The chemical variability of clinopyroxenes, their complex REE patterns and the dissociation between sample texture and clinopyroxene composition indicates a largely metasomatic origin. The most immediate evidence is the occurrences of clinopyroxene veins, most notably in sample 67-02E(1), which are almost exclusively associated with protogranular textures. As noted above, these veins have relatively well-equilibrated grain boundaries with the surrounding peridotite compared to the reaction patches, which implies they precede the reaction patches in the chronology of the samples. The trace element chemistry of clinopyroxenes in these veins (type I clinopyroxene) appears very similar to randomly distributed clinopyroxenes from several other Ritter peridotites, indicating that they share a similar metasomatic origin (Fig. 8). Whilst Type I patterns contain features which are typical of subduction-related fluids, such as positive Sr anomalies and negative Nb, Hf, Zr and Ti anomalies (Hawkesworth *et al.,* 1993; Elliott *et al.,* 1997), these may be compensated by opposite anomalies in orthopyroxene thus rendering them unreliable diagnostic tools. Based on the chronology of events though, it is most likely that these formed during some metasomatic event associated with the subduction event. This chronology is supported by the low temperatures recorded by the partitioning of V, Cr and Y between clinopyroxene and olivine, which requires that this period of metasomatism preceded the sub-solidus cooling (Fig. 13). A similar fluid was possibly responsible for the 'fossil' dunite and pyroxenite melt-rock reaction channels also preserved in the Ritter sample suite and described later. For example, the trace element composition and patterns of clinopyroxene from the pyroxenites are very similar to clinopyroxene in harzburgites (Fig. 8).

Downloaded from https://academic.oup.com/petrology/article-abstract/doi/10.1093/petrology/egx062/4523818
by University of Durham user
on 07 November 2017

Type II clinopyroxenes are characterised by sinusoidal REE patterns (Fig. 8). Similar REE patterns are commonly observed in low Ca garnets from cratonic mantle xenoliths (Stachel *et al.,* 1998; Stachel *et al.,* 2004; Simon *et al.,* 2007; Klein-BenDavid & Pearson, 2009; Gibson *et al.,* 2009; Gibson *et al.,* 2013), but are much rarer in spinel-facies clinopyroxene (for example, Scambelluri *et al.,* 2006). This clinopyroxene has distinctly lower HREE concentrations but similar LREE concentrations to those lacking sinusoidal REE patterns. A common interpretation of such patterns observed in cratonic peridotite garnets and diamond inclusions is the overprinting of a residual garnet signature with a strongly LREE-enriched metasomatic fluid (very high LREE/HREE). The 'humped' pattern from LREE to MREE would thus be attributed to interaction with this metasomatic agent, whilst the positive slope of the HREE would reflect the concentrations residual to an earlier partial melting event, preserved due to the low HREE concentrations in the fluid. We find this interpretation of partial melting followed by metasomatism to be consistent with the REE patterns displayed by the type II clinopyroxenes. The exact composition, nature and origin of the metasomatic agent responsible is difficult to constrain, given the scarcity of samples containing type II clinopyroxenes. Extended trace element patterns are similar to those for type I clinopyroxenes, albeit typically more extreme in trace element anomalies. Sample 67-02A(2) in particular contains clinopyroxenes with very strong negative Ti and HFSE anomalies and positive Sr anomalies. The overall similarity between the normalised trace element patterns of type I and type II clinopyroxenes implies that the two metasomatic agents may be linked. For example, it is possible that two end-member agents are present in the mantle wedge; a very LREE-rich/HFSE-depleted hydrous fluid and a more LREE-depleted silicate melt. The variation in the strength of particular trace element anomalies could thus reflect varying degrees of mixing between these end-member components.

Downloaded from https://academic.oup.com/petrology/article-abstract/doi/10.1093/petrology/egx062/4523818
by University of Durham user
on 07 November 2017

An important observation here though is that both distinct styles of metasomatism are found associated within this suite of arc peridotites and also global occurrences of cratonic peridotites, implying subduction-related fluids may have played a role in the formation of cratonic mantle.

A final clinopyroxene type (type III) is present in sample 67-02D(7), occurring in a single coarse vein (Fig.8). Such clinopyroxene is distinguished by lower Mg#, CaO and higher Al_2O_3. The REE and extended trace element patterns of Type III clinopyroxene is broadly similar to that of type I, except they are more enriched, with less extreme Ti anomalies. We interpret these to form in a similar way as type I clinopyroxene, but with a more evolved silicate melt as the metasomatising agent. Crystallisation of pyroxene within the mantle wedge (for example to form pyroxenite veins) would result in a decrease in Mg# and CaO and an increase in incompatible components in the residual melt.

Formation of dunites and pyroxenites

All three clinopyroxene populations described above formed through small degrees of metasomatic refertilisation of strongly depleted residual harzburgite. At the small scale, this process is capable of reversing the chemical and mineralogical features imposed by partial melting, by transforming harzburgite to lherzolite, an early stage of which is recorded by the Ritter samples. At the most extreme end of this process, however, is the complete transformation of peridotite into lithologies dominated by clinopyroxene and, or, orthopyroxene through reaction of residual phases with silica-rich melt, or the direct precipitation of new phases to form discrete bodies of pyroxenite. A related process but involving different melt compositions (for example, different silica contents) or reaction conditions may induce the reverse, dissolving pyroxenes in peridotite to form dunite (Kelemen *et al.,* 1992; Smith *et al.,* 1999), often bearing

Downloaded from https://academic.oup.com/petrology/article-abstract/doi/10.1093/petrology/egx062/4523818
by University of Durham user
on 07 November 2017

interstitial melt, clinopyroxene and, or, hydrous phases such as amphibole (Tursack & Liang, 2012; Tollan *et al.,* 2015). Both of these end-member refertillisation products are represented in the Ritter suite. As discussed above, the similar composition of pyroxenes from the harzburgites and pyroxenites implies that they formed as part of the same refertilisation process and therefore may have occurred at similar stages of the petrological evolution of the mantle beneath Ritter island. This is further supported by the equilibration temperatures, which, given the high degrees of melt-rock reaction, are lower than the apparent temperatures recorded by partially reacted harzburgites (Table 7).

The most fundamental question regarding the origin of the dunite examined in this study is whether it formed through a melt-rock reaction process or instead whether the samples represent residues of very high degrees of partial melting, beyond the point of orthopyroxene exhaustion. The very high olivine Mg# and spinel Cr# of dunite 67-02B(2) could be consistent with residues of mantle melting after orthopyroxene exhaustion (Herzberg, 2004) and are similar to values obtained for primitive basaltic phenocrysts from the Mariana arc (Tamura *et al.,* 2014), which were interpreted to be derived from crystallisation of a primary melt in equilibrium with residual dunite. However, we find partial melting to be an unsatisfactory explanation for the Ritter dunites, for a number of reasons. Firstly, to produce a dunite residue would require extremely high degrees of partial melting, in excess of 40 % (Herzberg, 2004; Berstein *et al.,* 2007), which is significantly higher than our estimates from the moderately incompatible trace element contents of residual orthopyroxenes in this study. Secondly, the incompatible trace element composition of the olivine in dunite is very similar to that of olivine in residual harzburgite. Of particular significance are Ti and P, which are not strongly affected by sub-solidus cooling (Witt-Eickschen & O'Neill, 2005; De Hoog *et al.,* 2010) and more likely to

Downloaded from https://academic.oup.com/petrology/article-abstract/doi/10.1093/petrology/egx062/4523818
by University of Durham user
on 07 November 2017

record conditions of melting, are similar or slightly higher in the olivine in dunite. Thirdly, the dunite, as with the pyroxenite is a subordinate assemblage to the harzburgites. If regional mantle potential temperatures were high enough to generate dunite residues it would be expected that they should be the dominant lithology found beneath Ritter. Finally, and most compellingly, is that the composition and occurrence of dunite is entirely consistent with studies of dunite channels in harzburgitic ophiolites and mantle xenoliths with a purported arc-origin (Parkinson *et al.,* 2003; Suhr *et al.,* 2003; Morgan *et al.,* 2008; Batanova *et al.,* 2011; Morishita *et al.,* 2011; Pirard *et al.,* 2013). These studies showed that, unlike dunite channels in lherzolitic mantle, olivine and spinel compositions evolve to higher Mg# and Cr# respectively during the process of melt-rock reaction in harzburgitic mantle, which is the case for the Ritter samples (Fig. 4; Fig. 5). Olivine in the Ritter dunite also has lower NiO contents for the same Mg# as olivine in harzburgite, similar to results from the aforementioned studies (Fig. 4). This collective evidence thus suggests that the most plausible origin for dunite is that it represents fragments of melt channels, rather than residues of melting.

A further important question, as with the pyroxenite, is the relative timing at which the dunite formed. Dunite sample 67-02D(3) records an olivine-spinel temperature as low as the protogranular harzburgites, indicating that it has undergone the same cooling history. This is supported further by the highly depleted concentrations of temperature-sensitive elements such as Al, Cr and Y in olivine from this sample (Table 6) and the identical composition of olivine in the dunite vein and the surrounding 'primary' dunite. Since the process of melt-rock reaction results in enrichment of incompatible trace elements in olivine (Tollan *et al.,* 2015), a significant period of time must have passed in order for the dunite vein and 'primary' dunite to equilibrate, not just with each other but also with the surrounding ambient mantle. If this is indeed the case,

Downloaded from https://academic.oup.com/petrology/article-abstract/doi/10.1093/petrology/egx062/4523818
by University of Durham user
on 07 November 2017

then this demonstrates that fine-grained domains in otherwise coarse-grained mantle rocks may be able to survive during sustained periods of residence in the mantle. The survival of this heterogeneous texture may have been facilitated by the intermixed spinel since the presence of a second phase in an otherwise homogeneous fine-grained matrix is known to inhibit crystal coarsening (Olgaard & Evans, 1986; Evans *et al.,* 2001; Linckens *et al.,* 2011).

Dunite sample 67-02B(2) records considerably higher olivine-spinel temperatures (1130-1230 °C), similar to those of the reaction patches (as discussed later). Furthermore, this sample contains traces of glass surrounding coarse spinel grains which contains small pockets of a second olivine composition with a lower (although still high) Mg# of 91-92. We suggest that this sample represents a fossil dunite channel formed through a previous episode of melt-rock reaction, which was subsequently exploited by a more recent melt percolation event. This resulted in the localised modification of spinel and olivine rims to less refractory compositions, and heating to temperatures close to the basalt liquidus. We note that the composition of secondary olivine is very similar to secondary olivine formed in the harzburgite-dunite transition sample 67-02A(3), discussed in detail by Tollan *et al.,* (2015) and included in Table 2 for reference. It is therefore highly likely that the same melt composition was responsible for the secondary textures in both samples.

Sub-solidus cooling

The unusually broad range of temperatures recorded within individual samples of the Ritter suite allows a cooling rate to be estimated. Each of the geothermometers used in this study has a closure temperature, which is the temperature at which diffusion of the principle components involved in the temperature-sensitive exchange reaction becomes essentially zero, resulting in

Downloaded from https://academic.oup.com/petrology/article-abstract/doi/10.1093/petrology/egx062/4523818
by University of Durham user
on 07 November 2017

'freezing' of the temperature at effective diffusion arrest. For samples which have experienced a prolonged cooling event, temperatures calculated using geothermometers with different closure temperatures should therefore record a range of temperatures proportional to the rate of cooling. To calculate this, firstly the temperatures calculated using four different methods (Fe-Mg exchange between olivine and spinel and Fe-Mg, Yb and Ce exchange between pyroxenes) were compared against the diffusivity of these components in olivine and clinopyroxene respectively. Other geothermometers were not included due to a lack of published diffusion data. There is a good positive correlation, supportive of an important kinetic control (Fig. 14). The slope of the best fit to this correlation is proportional to the cooling rate. To calculate this we used Dodson's equations for closure temperature (Dodson, 1973):

$$T_c = E/R[ln(A\tau D_0/a^2)]$$

where T_c is the closure temperature; E is the activation energy of diffusion; R is the ideal gas constant; A is a geometric constant (55 for spherical grains); $D_0$is the diffusion constant; a is the grain radius and τ is the cooling rate constant:

$$\tau = -RT_c^2/[E(dT/dt)]$$

where dT/dt is the cooling rate. These equations were solved for each temperature estimate from the four geothermometers simultaneously by performing a least squares regression to find the value of dT/dt that resulted in the best match between each calculated value of T_c and the respective geothermometry results. The result is sensitive to grain size which in the Ritter samples varies between different phases and samples. For an average grain radius of 2 mm, representative of the Ritter suite, the best-fit cooling rate is 20 °C/Ma. The model was also run with additional grain radii from 1 mm to 3 mm, which resulted in cooling rates ranging from 79

Downloaded from https://academic.oup.com/petrology/article-abstract/doi/10.1093/petrology/egx062/4523818
by University of Durham user
on 07 November 2017

°C/Ma to 9 °C/Ma respectively. The study of Dygert & Liang (2015) employed a similar methodology to estimate cooling rates for exhumed mantle from a range of tectonic settings. They calculated a wide spectrum of cooling rates (with the caveat that some of this variation may be due to varying grain sizes), but in general found that peridotites with a supra-subduction zone (SSZ) affinity had greater disparity between thermometers with different closure temperatures and hence slower cooling rates. Our data for the Ritter peridotites are in good agreement with their conclusions, with cooling rates at the slowest estimates of their study, overlapping with SSZ peridotites (Fig 14b). The slow cooling rates of the Ritter samples compared to peridotites from spreading centres and even other SSZ settings is best explained by prolonged periods of time in zones of active melting. Mantle beneath spreading centres on the other hand is rapidly transported away from melting regions, is typically overlain by thinner crust and experiences additional cooling by hydrothermal processes (Dygert & Liang, 2015). To understand in more detail the thermal history of the Bismarck microplate, our data can be compared to cooling rates calculated by Franz *et al.,* (2002) for peridotites from the nearby Vitiaz West-Melanesian arc system. Whilst this arc system is no longer active, it is thought to have perhaps played an important role in the petrogenesis of the Bismarck microplate (Woodhead *et al.,* 1998); hence, the relationship between this extinct system and the modern subduction system comprising the West Bismarck and New Britain island arcs is important to understand. The peridotite samples studied by Franz *et al.,* (2002) experienced an extremely slow cooling rate of 0.1-1 °C/Ma, calculated from Ca diffusion in olivine. Whilst our cooling rate calculations have considerable uncertainty (± 17 °C/Ma), they are still clearly higher than the estimate of Franz *et al.* (2002) by at least an order of magnitude, indicating that the mantle beneath Ritter followed a more rapid period of cooling after the extinction of the Vitiaz West-Melanesian arc. One explanation for this

Downloaded from https://academic.oup.com/petrology/article-abstract/doi/10.1093/petrology/egx062/4523818
by University of Durham user
on 07 November 2017

is that cooling was accelerated by the opening of the nearby Manus fast-spreading centre and consequential formation of the Manus Basin, moving the mantle sampled in this study rapidly away from the earlier locus of melting. However, the associated development of new subduction systems at West Bismarck and New Britain may have perturbed this increase in cooling rate somewhat, maintaining the overall slow cooling rates compared to global peridotites (Dygert & Liang, 2015).

Trace element redistribution during cooling

Given the clear and variable impact of sub-solidus cooling on the inter-mineral distribution of trace elements, it is important to assess whether this has a significant impact on the result of the melting model presented above, which assumes the measured concentrations are the same as during the conditions of partial melting. To do this, the pyroxene-melt and olivine-melt partitioning models of Liang *et al.* (2013) and Sun & Liang (2013) were combined to calculate mineral-mineral partition coefficients for Y and Yb over the temperature range 1300-600 °C. Using these values, the concentrations in clinopyroxene, orthopyroxene and olivine were calculated over this temperature range, assuming a closed system and using a bulk concentration estimated from the average measured mineral compositions and modal proportions of 74 % olivine, 25 % orthopyroxene and 1 % clinopyroxene. In this case, we have assumed the clinopyroxene was present during the full extent of sub-solidus cooling in order to present a 'worst case' scenario. The results of this exercise are shown in Fig. 15, with concentrations expressed as percentages relative to the initial concentrations in each phase. As anticipated, the composition of olivine is highly sensitive to temperature, retaining only 2.5 % and 0.5 % of the initial concentrations of Yb and Y, respectively, by 600 °C. Even at 700 °C only 2 % and 7 % of these elements remain. The important implications here are the confirmation that olivine trace

Downloaded from https://academic.oup.com/petrology/article-abstract/doi/10.1093/petrology/egx062/4523818
by University of Durham user
on 07 November 2017

element composition is a useful monitor of equilibration temperature (De Hoog *et al.,* 2010), and also that at near-solidus conditions olivine can store a significant inventory of the total trace element budget (nearly 10 % of Yb at 1300 °C), which is not apparent from simply measuring olivine in its final equilibration state. Studies that utilise the chemistry of olivine in slowly cooled systems to infer changes in melt composition, for example in the mantle-crustal layers of ophiolites, must take into account this cooling effect. Trends observed between olivines in, for example, peridotite, dunite and gabbroic layers, may simply be related to differences in the mineralogical environment during cooling. In contrast to olivine, clinopyroxene becomes strongly enriched during the cooling process, gaining an additional 170-190 % of both Yb and Y by 900 °C, similar to the results obtained by Sun & Liang (2014) and McCoy-West *et al.* (2015). If kinetics permitted, by 600 °C clinopyroxene would have gained approximately 400-600 % of these elements. Orthopyroxene displays more complex behaviour, but in general is less susceptible to cooling. At high temperatures it becomes slightly more enriched before becoming depleted at lower temperatures. This switch from enrichment to depletion is due to the way that $D^{cpx/opx}$, $D^{opx/ol}$ and $D^{cpx/ol}$ each change with temperature, and occurs at lower temperatures for less incompatible elements. This means that by ~950 °C (the calculated clinopyroxene/orthopyroxene REE closure temperature for the Ritter samples), orthopyroxenes have lost only ~10 % Y and gained ~20 % Yb. This correction was combined with a further small correction for exchange with olivine alone, down to 600 °C in order to be consistent approximately with the distribution of Y between olivine and orthopyroxene compared to the data of Witt-Eickschen & O'Neill (2005). The impact when applied to the measured data was overall insignificant for the conclusions drawn from the partial melting exercise (Fig. 11).

Formation of orthopyroxene veins and reaction patches

Downloaded from https://academic.oup.com/petrology/article-abstract/doi/10.1093/petrology/egx062/4523818
by University of Durham user
on 07 November 2017

Whilst minerals associated with protogranular texture provide insights into the early melting, metasomatic and cooling histories of these samples, minerals in reaction patches/veins of the harzburgites, pyroxenites and dunites record evidence of a subsequent process. These features are very heterogeneous, not just between samples from the same locality, but also within individual hand specimens, indicating that this process was localised and occurred on timescales short enough to preserve relatively unstable features such as glassy patches, sutured grain boundaries, incomplete mineral replacement reactions and fine-grained crystal domains (Fig. 2; Fig. 3). Many of the features of the reaction textures are commonly observed in other suites of arc peridotites, most notably veins and patches of secondary orthopyroxene forming at the expense of olivine during reaction with a silicate melt or aqueous fluid ($Mg_2SiO_4^{Olivine} + SiO_2^{Fluid} = Mg_2Si_2O_6^{Opx}$; Franz *et al.,* 2002; Arai *et al.,* 2004; Berly *et al.,* 2006; Bryant *et al.,* 2007; Ionov, 2010; Bénard & Ionov, 2013).

The origins of glass and clinopyroxene-bearing reaction patches in peridotites remain controversial. The likely mechanisms are: (i) the reaction between residual peridotite phases and an infiltrating silicate melt; (ii) the breakdown of amphibole, either by infiltration of melt in the mantle or during re-heating and decompression upon exhumation (Schiano, 1999; Shaw, 2009). Our favoured interpretation for these samples is the former, since the mineral assemblage in the reaction patches (orthopyroxene-glass-clinopyroxene) is different to those inferred as products of amphibole breakdown (olivine-glass-clinopyroxene ± amphibole; Shaw, 2009). The assumed high water activity of the host arc magma should help preserve any amphibole during ascent, hence the absence of this phase in the exhumed Ritter samples most likely indicates it was not stable in the mantle source, rather than being lost during magmatic transport. Furthermore, many of the textural features observed in the Ritter reaction patches, particularly sieve-textured spinel,

Downloaded from https://academic.oup.com/petrology/article-abstract/doi/10.1093/petrology/egx062/4523818
by University of Durham user
on 07 November 2017

were reproduced experimentally by Shaw & Dingwell (2008) by reacting silicate melt with peridotite under appropriate conditions for the upper mantle.

There are distinct geochemical differences between peridotite samples containing reaction patches or veins and those that do not. Firstly, temperatures calculated using fine-grained clinopyroxene and orthopyroxene from reaction patches are 1220-1260 ºC, substantially higher than the equilibration temperatures of residual phases (Table 7). These temperatures are above estimates of the wet peridotite solidus at spinel-facies pressures (Grove *et al.,* 2012), but below the dry peridotite solidus, assuming a depleted source (McDade *et al.,* 2003a), supporting the idea that percolation of a hydrous melt was responsible for the reaction textures observed. Secondly, the compositions of spinel and olivine are distinctly different in samples bearing reaction textures, in particular those with interstitial glass. This is most apparent in the olivine trace element dataset, because the rapid diffusivity of elements in olivine means it is more likely to record late-stage perturbations in bulk composition and, or, temperature compared to pyroxene (Cherniak & Liang, 2007; De Hoog *et al.,* 2010; Spandler & O'Neill, 2010; Foley *et al.,* 2013; Tollan *et al.,* 2015) . This is particularly true for 'cold' ambient mantle such as the Ritter suite where the unusually large temperature gradient with the reacting melt resulted in rapid diffusive re-equilibration of olivine grains, resulting in distinct trends in composition (Tollan *et al.,* 2015). Olivines associated with residual textures have very low trace element concentrations which are a function of both the very low equilibration temperatures and the high degrees of melt extraction. They form a tight cluster in compositional space confirming they have experienced negligible influence from reacting melts or the host magma during ascent (Fig. 9). Olivines associated with reaction textures fall on a narrow array which extends away from those associated with residual textures, with over an order of magnitude enrichment in some trace

Downloaded from https://academic.oup.com/petrology/article-abstract/doi/10.1093/petrology/egx062/4523818
by University of Durham user
on 07 November 2017

elements (particularly sensitive are Na, Ca, Cr, Ti and Y). Despite differences in the types of reaction texture, the trends in olivine trace element space are nearly identical between samples, which indicates that the concentrations of these elements in the melt, and temperature of reaction, were similar. However, there are clear indications from the textures that the major element composition of these melts must have been different. For example, whilst the reaction of olivine and melt to form orthopyroxene is the most common reaction observed, sample 67-02D(4) shows the reaction of orthopyroxene to form a second composition of orthopyroxene intermingled with the original composition, with no evidence for olivine consumption (Fig. 3e). Combined with the evidence for similarly recent dunite formation, this clearly indicates that a variety of melt compositions were present in the shallow mantle wedge in close spatial proximity, although whether they were related to each other genetically is beyond the scope of this study.0

Due to the incompatibility of many trace elements in orthopyroxene and clinopyroxene, the trace element composition of bulk ablations of reaction patches should be dominated by the small proportions of interstitial glass, with orthopyroxene and clinopyroxene acting merely as diluents. Hence the data should approximate the trace element composition of the melt responsible for their formation, with the exception of the HREE, which are only moderately incompatible in the pyroxenes. This is confirmed when comparing data from different ablations of reaction patches within the same sample, which show significant variations in concentration but relatively constant element ratios. This is best explained by variable amounts of glass incorporated in each ablation. Comparing the data for reaction patches and residual orthopyroxene from the same sample, there are large enrichments in incompatible elements, which are strongest for highly incompatible elements, particularly the LILE and Sr. The REE

Downloaded from https://academic.oup.com/petrology/article-abstract/doi/10.1093/petrology/egx062/4523818
by University of Durham user
on 07 November 2017

show systematically greater levels of enrichment from moderately incompatible HREE through to highly incompatible LREE, whereas Ti and the HFSE show much lower levels of enrichment in the reaction patches compared to neighbouring elements of similar compatibility. These trace element signatures are characteristic of island arc basalts (Elliott *et al.,* 1997), supporting our interpretation that the observed textural and chemical features were produced in a sub-arc setting.

Summary of the petrological evolution of the West Bismarck mantle

Our detailed geochemical study reveals a complex, multi-stage history for the mantle underlying the West Bismarck island arc, which is not entirely obvious through simple petrographic inspection of the peridotites or through geochemical studies of lavas (Woodhead *et al.,* 1998; Woodhead *et al.,* 2010; Cunningham *et al.,* 2012). The earliest stage of petrogenesis which can be clearly identified is a hydrous melting episode within an 'ancient' subduction system (Fig.16). This generated the highly depleted HREE compositions of orthopyroxene (relative to melting at spreading centres), high Mg# and low Al_2O_3 content of orthopyroxene, highly forsteritic olivine and high Cr# of spinel associated with a protogranular texture. It is unclear from the major and trace element systematics where this subduction system was in relation to the present day West Bismarck arc; however, it is possible that the melting episode was caused by subduction in the north associated with the now extinct Manus/Kilinailau trench. This would be in agreement with Woodhead *et al.* (1998) who studied lavas erupted along the neighbouring New Britain island arc and interpreted anomalously radiogenic Sr and Pb isotope signatures to reflect tapping of a mantle source enriched by this previous subduction event. Following this melting event, the mantle wedge was exposed to a variety of distinct fluid compositions, resulting in modal and cryptic metasomatism. This is most obvious by the presence of 'fossil' dunite melt channels, relatively well-equilibrated veins of clinopyroxene and multiple clinopyroxene chemistries,

Downloaded from https://academic.oup.com/petrology/article-abstract/doi/10.1093/petrology/egx062/4523818
by University of Durham user
on 07 November 2017

including a population displaying rare sinusoidal REE patterns. The trace element composition of these different clinopyroxene populations likely requires mixing of fluids originating from different parts of the slab or mantle. After melting and metasomatism, the mantle cooled rapidly from initial temperatures above the wet peridotite solidus down to unusually cold equilibration temperatures of ~650 °C. This cooling episode was rapid enough to preserve high closure temperatures calculated from clinopyroxene-orthopyroxene chemical equilibria, but slow enough to allow diffusive equilibration of rapidly diffusing components in olivine and spinel, and was largely responsible for the highly depleted trace element concentrations in olivine associated with protogranular textures. Whilst accurate and precise barometry is not possible for spinel peridotites, the change in temperature requires considerable accompanying decompression from the elevated pressures of melting at asthenospheric depths to the shallow lithospheric mantle. During this period of cooling and decompression, the ambient mantle entered the present day West Bismarck arc system. The activity related to this period of petrogenesis is clearly observed texturally and chemically in a number of peridotite samples, which experienced variable degrees of silicate melt-rock reaction, producing patches and veins of secondary orthopyroxene with interstitial clinopyroxene and glass, and occasional recrystallization to form porphyroclastic textures (Tollan *et al.,* 2015). Significantly, the nature of the reactions taking place vary considerably between samples, as observed through the resultant secondary phase assemblages, indicating a range of distinct melts present in the shallow lithospheric sub-arc mantle. Chemical changes associated with this process are higher equilibration temperatures (up to 1260 ºC), trace element disequilibria in olivine and elevated spinel Cr#. The preservation of ambient mantle chemistry and textures in the Ritter peridotite suite, alongside the reaction textures, indicates that melt infiltration was isolated mainly to channels and veins and probably occurred on a timescale

Downloaded from https://academic.oup.com/petrology/article-abstract/doi/10.1093/petrology/egx062/4523818
by University of Durham user
on 07 November 2017

shortly before formation and entrainment of the xenoliths in the host magma (Tollan *et al.,* 2015).

Comparisons with cratonic mantle

Many of the geochemical features of cratonic mantle have been attributed to subduction-related processes and thus comparison with samples of sub-arc mantle provides a means of testing and refining this hypothesis. An important distinguishing aspect of many cratonic xenoliths is an elevated modal abundance of orthopyroxene and whole-rock Si/Mg ratios relative to melt depletion trends. One interpretation of this signature is that it reflects metasomatism within a subduction zone by Si-rich, slab-derived fluids (Parman *et al.,* 2004; Simon *et al.,* 2007; Pearson & Wittig, 2008; Tappe *et al.,* 2011). The Ritter peridotites, similar to other arc-related peridotites, contain clear evidence for the formation of secondary orthopyroxene and clinopyroxene through metasomatism or melt-rock reaction (Arai & Ishimaru, 2008), confirming that this is likely to be a ubiquitous process within the shallow lithospheric arc mantle. The magnitude of this enrichment however, is difficult to estimate from the narrow view provided by even a highly populous xenolith suite such as Ritter and thus it is difficult to establish just how widespread such silica enrichment may be in the convecting mantle wedge. An additional and important feature, perhaps unique amongst previously studied arc peridotites compared with the Ritter peridotite suite, is the occurrence of sinusoidal clinopyroxene REE patterns which are commonly observed in cratonic mantle mineral phases (Stachel *et al.,* 1998; Stachel *et al.,* 2004; Simon *et al.,* 2007; Klein-BenDavid & Pearson, 2009; Gibson *et al.,* 2009; Gibson *et al.,* 2013). Again, whilst the occurrence of this signature is relatively rare in the Ritter suite, it does indicate that fluids of similar composition are being generated within modern subduction zone settings. This is reinforced by some additional features of Type II Ritter clinopyroxene, in particular the

Downloaded from https://academic.oup.com/petrology/article-abstract/doi/10.1093/petrology/egx062/4523818
by University of Durham user
on 07 November 2017

very low $(Ti/Eu)_N$ which is characteristic of carbonatitic fluids, a commonly inferred fluid type in cratonic mantle metsomatism (Gibson *et al.,* 2013).

Despite these similar metasomatic features, notable differences exist between the Ritter peridotites and typical cratonic peridotites. Perhaps most significant amongst these is the Mg# of olivine, which shows considerable variation between mantle domains, a function principally of the degree of partial melting (Berstein *et al.,* 2007). Cratonic mantle olivine has an average Mg# of 92.5-92.8, significantly higher than average abyssal peridotite olivine (Mg# 90.8; Pearson & Wittig, 2008), reflecting partial melting up to the point of clinopyroxene exhaustion at elevated pressures (Herzberg, 2004). Ritter olivine on the other hand, averages Mg# 91.5, overlapping with the extended range of both mantle types, consistent with shallow pressures of melting up to clinopyroxene exhaustion, as estimated from our modelling of orthopyroxene trace element concentrations. Given that both Ritter and a number of other arc samples, such as those from Kamchatka (Ionov, 2010), have experienced melting up to the point of clinopyroxene exhaustion, similar to cratonic mantle, the higher Mg# of cratonic mantle is more likely to reflect different pressures of melting. Assuming that arc peridotite xenoliths are biased towards shallower portions of the melting zone in the mantle wedge (kimberlite extraction of cratonic mantle xenoliths facilitates sampling to much greater depths; Pearson *et al.,* 2003), this does not necessarily pose a problem for the hypothesis of subduction zone influence in the generation of cratonic mantle. Hence, we conclude that whilst there remains no conclusive links between arc and cratonic mantle samples, compelling lines of evidence from both melting histories and modes of metasomatism point towards several common processes, at least from the petrographic and geochemical perspective provided by xenoliths samples.

Downloaded from https://academic.oup.com/petrology/article-abstract/doi/10.1093/petrology/egx062/4523818
by University of Durham user
on 07 November 2017

ACKNOWLEDGEMENTS

This project was the brainchild of Jon Davidson, who supervised the PhD of Peter Tollan. Jon died during the writing and publication of this manuscript. We dedicate this paper to Jon in recognition of his significant contribution to our understanding of subduction zone magmatism.

The authors gratefully acknowledge Sarlae McAlpine and Ian Chaplin for production of peridotite billets and thin sections, Jung-Woo Park for assistance with LA-ICP-MS measurements, Bob Rapp and Pierre Lanari for assistance with the electron microprobe and Laure Gauthiez Putallaz and Morgan Williams with the SEM. Members of the Petrology Group at ANU and Volcanology Group at Durham are thanked for advice, particularly Hugh O'Neill, Greg Yaxley, Mike Jollands and Helen Williams. Ian Parkinson and Kevin Burton are thanked for their feedback on an earlier version of this work. We thank Simon Turner for the editorial handling and Michael Bizimis, Yoshihiko Tamura and John Shervais for detailed reviews. This work could not have been completed without the support of Karl Dilkington.

APPENDIX

The following equations were used for the partial melting model.

$$C_{res} = C_0 \frac{1}{1-X}\left\{1 - \frac{X[P+\Phi(1-P)]}{D_0+\Phi(1-P)}\right\}^{\frac{1}{[\Phi+(1-\Phi)P]}}$$

(Zou 1998), where C_{res} is the concentration in the bulk residue, C_0 is the initial concentration; X is the fraction of extracted melt; P is the relative proportions of minerals entering the melt according to the chosen melting reaction; D_0 is the bulk partition coefficient of the source

Downloaded from https://academic.oup.com/petrology/article-abstract/doi/10.1093/petrology/egx062/4523818
by University of Durham user
on 07 November 2017

calculated from the sum of mineral-melt partition coefficients multiplied by the modal abundance of each phase; Φ is the critical mass porosity of the residue, related to X and melt fraction, F, through the equation $X = F - \Phi$

The concentration of elements in residual orthopyroxene was then calculated according to the equation:

$$C_{opx} = \frac{D^{opx/melt}}{D^{bulk/melt}} C_{res}$$

where

$$D^{bulk/melt} = (D_0 - PF)/(1 - F)$$

and

$$D_0 = \sum D_i x_i$$

where D_i is the mineral-melt partition coefficient for mineral i and x_i is the modal proportion of phase i.

The anhydrous lherzolite melting reaction was from Baker & Stolper (1994):

0.71 cpx + 0.38 opx + 0.13 spinel = 0.22 olivine + 1 melt

The hydrous lherzolite melting reaction was from Gaetani & Grove (1998):

0.62 cpx + 0.51 opx + 0.12 spinel = 0.25 olivine + 1 melt

The hydrous harzburgite melting reaction was from Parman & Grove (2004):

0.23 olivine + 0.87 opx = 1 melt

Downloaded from https://academic.oup.com/petrology/article-abstract/doi/10.1093/petrology/egx062/4523818
by University of Durham user
on 07 November 2017

REFERENCES

Abbott, L.D., Silver, E.A., Thompson, P.R., Filewicz, M.V., Schneider, C., Abdoerrias, (1994). Stratigraphic constraints on the development and timing of arc-continent collision in northern Papua New Guinea. *Journal of Sedimentary Research* **64**, 169-183

Annen, C., Blundy, J.D., Sparks, R.S.J., (2006). The Genesis of Intermediate and Silicic Magmas in Deep Crustal Hot Zones. *Journal of Petrology* **47**, 505-539

Arai, S. (1994). Characterization of spinel peridotites by olivine-spinel compositional relationships: Review and interpretation. *Chemical Geology* **113**, 191-204

Arai, S., Takada, S., Michibayashi, K., Kida, M. (2004). Petrology of Peridotite Xenoliths from Iraya Volcano, Philippines, and its Implication for Dynamic Mantle-Wedge Processes. *Journal of Petrology* **45**, 369-389

Arai, S. & Ishimaru, S. (2008). Insights into Petrological Characteristics of the Lithosphere of Mantle Wedge beneath Arcs through Peridotite Xenoliths: a Review. *Journal of Petrology* **49**, 665-695

Baker, M.B. & Stolper, E.M. (1994). Determining the composition of high-pressure mantle melts using diamond aggregates. *Geochimica Cosmochimica Acta* **58**, 2811-2827

Batanova, V.G., Belousov, I.A., Savelieva, G.N., Sobolev, A.V. (2011). Consequences of Channelized and Diffuse Melt Transport in Supra-subduction Zone Mantle: Evidence from the Voykar Ophiolite (Polar Urals). *Journal of Petrology* **52**, 2483-2521

Downloaded from https://academic.oup.com/petrology/article-abstract/doi/10.1093/petrology/egx062/4523818
by University of Durham user
on 07 November 2017

Bénard, A. & Ionov, D.A. (2013). Melt- and Fluid-Rock Interaction in Supra-Subduction Lithospheric Mantle: Evidence from Andesite-hosted Veined Peridotite Xenoliths. *Journal of Petrology* **54**, 2339-2378

Berly, T.J., Hermann, J., Arculus, R.J., Lapierre, H. (2006). Supra-subduction Zone Pyroxenites from San Jorge and Santa Isabel (Solomon Islands). *Journal of Petrology* **47**, 1531-1555

Bernstein, S., Hanghøj, K., Kelemen, P.B. (2006). Ultra-depleted, shallow cratonic mantle beneath West Greenland: dunitic xenoliths from Ubekendt Ejland. *Contributions to Mineralogy and Petrology* **152**, 335-347

Bernstein, S., Kelemen, P.B., Hanghøj, K. (2007). Consistent olivine Mg# in cratonic mantle reflects Archean mantle melting to the exhaustion of orthopyroxene. *Geology* **35**, 459-462

Bizimis, M., Salters, V.J.M., Bonatti, E. (2000). Trace and REE content of clinopyroxenes from supra-subduction zone peridotites. Implications for melting and enrichment processes in island arcs. *Chemical Geology* **165**, 67-85

Blundy, J. & Wood, B. (1994). Prediction of crystal-melt partition-coefficients from elastic-moduli. *Nature* **372**, 452-454

Brandon, A.D. & Draper, D.S. (1996). Constraints on the origin of the oxidation state of mantle overlying subduction zones: An example from Simcoe, Washington, USA. *Geochimica et Cosmochimica Acta* **60**, 1739-1749

Downloaded from https://academic.oup.com/petrology/article-abstract/doi/10.1093/petrology/egx062/4523818
by University of Durham user
on 07 November 2017

Brey, G.P. & Köhler, T. (1990). Geothermobarometry in Four-phase Lherzolites II. New Thermobarometers, and Practical Assessment of Existing Thermobarometers. *Journal of Petrology* **31**, 1353-1378

Brunelli, D., Seyler, M., Cipriani, A., Ottolini, L., Bonatti, E. (2006). Discontinuous Melt Extraction and Weak Refertilization of Mantle Peridotites at the Vema Lithospheric Section (Mid-Atlantic Ridge). *Journal of Petrology* **47**, 745-771

Brunneli, D. & Seyler, M. (2010). Asthenospheric percolation of alkaline melts beneath the St. Paul region (Central Atlantic Ocean). *Earth and Planetary Science Letters* **289**, 393-405

Bryant, J.A., Yogodzinski, G.M., Churikova, T.G. (2007). Melt-mantle interactions beneath the Kamchatka arc: Evidence from ultramafic xenoliths from Shiveluch volcano. *Geochemistry, Geophysics, Geosystems* **8**, doi:10.1029/2006GC001443

Cherniak, D.J. & Liang, Y. (2007). Rare earth element diffusion in natural enstatite. *Geochimica et Cosmochimica Acta* **71**, 1324-1340

Coogan, L.A., Saunders, A.D., Wilson, R.N., (2014). Aluminium-in-olivine thermometry of primitive basalts: Evidence of an anomalously hot mantle source for large igneous provinces. *Chemical Geology* **368**, 1-10

Cunningham, H., Gill, J., Turner, S., Caulfield, J., Edwards, L., Day, S. (2012). Rapid magmatic processes accompany arc-continent collision: the Western Bismarck arc, Papua New Guinea. *Contributions to Mineralogy and Petrology* **164**, 789-804

Downloaded from https://academic.oup.com/petrology/article-abstract/doi/10.1093/petrology/egx062/4523818
by University of Durham user
on 07 November 2017

Davis, F.A., Humayun, M., Hirschmann, M.M., Cooper, R.S., (2013). Experimentally determined mineral/melt partitioning of first-row transition elements (FRTE) during partial melting of peridotite at 3 GPa. *Geochimica et Cosmochimia Acta* **104**, 232-260

De Hoog, J.C.M., Gall, L., Cornell, D.H. (2010). Trace-element geochemistry of mantle olivine and application to mantle petrogenesis and geothermobarometry. *Chemical Geology* **270**, 196-215

Dodson, M.H. (1973). Closure temperature in cooling geochronological and petrological systems. *Contributions to Mineralogy and Petrology* **40**, 259-274

Dohmen, R., Chakraborty, S., (2007). Fe-Mg diffusion in olivine II: point defect chemistry, change of diffusion mechanisms and a model for calculation of diffusion coefficients in natural olivine. *Physics and Chemistry of Minerals* **34**, 409-430

Dygert, N. & Liang, Y. (2015) Temperatures and cooling rates recorded in REE in coexisting pyroxenes in ophiolitic and abyssal peridotites. *Earth and Planetary Science Letters* **420**, 151-161

Elliott, T., Plank, T., Zindler, A., White, W., Bourdon, B. (1997). Element transport from slab to volcanic front at the Mariana arc. *Journal of Geophysical Research* **102**, 14991-15019

Evans, B., Renner, J., Hirth, G. (2001). A few remarks on the kinetics of static grain growth in rocks. International. *Journal of Earth Sciences* **90**, 88-103

Foley, S.F., Prelevic, D., Rehfeldt, T., Jacob, D.E. (2013). Minor and trace elements in olivines as probes into early igneous and mantle melting processes. *Earth and Planetary Science Letters* **363**, 181-191

Downloaded from https://academic.oup.com/petrology/article-abstract/doi/10.1093/petrology/egx062/4523818
by University of Durham user
on 07 November 2017

Franz, L., Becker, K-P., Kramer, W., Herzig, P.M. (2002). Metasomatic Mantle Xenoliths from the Bismarck Microplate (Papua New Guinea)- Thermal Evolution, Geochemistry and Extent of Slab-induced Metasomatism. *Journal of Petrology* **43**, 315-343

Gaetani, G. & Grove, T. (1998). The influence of water on melting of mantle peridotite. *Contributions to Mineralogy and Petrology* **131**, 323-346

Gill, J.B., Morris, J.D., Johnson, R.W., (1993). Timescale for producing the geochemical signature of island-arc magmas: U-Th-Po and Be-B systematics in recent Papua New Guinea lavas. *Geochimica et Cosmochimica Acta* **57**, 4269-4283

Grove, T.L., Till, C.B., Krawczynski, M.J. (2012). The Role of H_2O in Subduction Zone Magmatism. *Annual Reviews of Earth and Planetary Science* **40**, 413-439

Hawkesworth, C.J., Gallagher, K., Hergt, J.M., McDermott, F. (1993). Mantle and slab contributions in arc magmas. *Annual Reviews of Earth and Planetary Science* **21**, 175-204

Heinonen, J.S., Jennings, E.S., Riley, T.R., (2015). Crystallisation temperatures of the most Mg-rich magmas of the Karoo KIP on the basis of Al-in-olivine thermometry. *Chemical Geology* **411**, 26-35

Hellebrand, E., Snow, J.E., Hoppe, P., Hofmann, A.W. (2002). Garnet-field Melting and Late-stage Refertilization in 'Residual' Abyssal Peridotites from the Central Indian Ridge. *Journal of Petrology* **43**, 2305-2338

Hellebrand, E., Snow, J.E., Mostefaoui, S., Hoppe, P. (2005). Trace element distribution between orthopyroxene and clinopyroxene in peridotites from the Gakkel Ridge: a SIMS and NanoSIMS study. *Contributions to Mineralogy and Petrology* **150**, 486-504

Downloaded from https://academic.oup.com/petrology/article-abstract/doi/10.1093/petrology/egx062/4523818
by University of Durham user
on 07 November 2017

Herzberg, C. (2004). Geodynamic Information in Peridotite Petrology. *Journal of Petrology* **45**, 2507-2530

Gaetani, G.A., Grove, T.L. (1998). The influence of water on melting of mantle peridotite. *Contributions to Mineralogy and Petrology* **131**, 323-346Gibson, S.A., Malarkey, J., Day, J.A. (2008). Melt Depletion and Enrichment beneath the Western Kaapvaal Craton: Evidence from Finsch Peridotite Xenoliths. *Journal of Petrology* **49**, 1817-1852

Gibson, S.A., McMahon, S.C., Day, J.A., Dawson, J.B. (2013). Highly Refractory Lithospheric Mantle beneath the Tanzanian Craton: Evidence from Lashaine Pre-metasomatic Garnet-bearing Peridotites. *Journal of Petrology* **54**, 1503-1546

Grégoire, M., McInnes, B.I.A., O'Reilly, S.Y. (2001). Hydrous metasomatism of oceanic sub-arc mantle, Lihir, Papua New Guinea Part 2. Trace element characteristics of slab-derived fluids. *Lithos* **59**, 91-108

Grove, T.L., Till, C.B., Krawczynski, M.J. (2012). The Role of H_2O in Subduction Zone Magmatism. *Annual Reviews of Earth and Planetary Science* **40**, 413-439

Ionov, D.A. (2010). Petrology of Mantle Wedge Lithosphere: New Data on Supra-Subduction Zone Peridotite Xenoliths from the Andesitic Avacha Volcano, Kamchatka. *Journal of Petrology* **51**, 327-361

Ishimaru, S., Arai, S., Ishida, Y., Shirasaka, M., Okrugin, V.M. (2007). Melting and Multi-stage Metasomatism in the Mantle Wedge beneath a Frontal Arc Inferred from Highly Depleted Peridotite Xenoliths from the Avacha Volcano, Southern Kamchatka. *Journal of Petrology* **48**, 395-433

Downloaded from https://academic.oup.com/petrology/article-abstract/doi/10.1093/petrology/egx062/4523818
by University of Durham user
on 07 November 2017

Jean, M.M., Shervais, J.W., Choi, S-H., Mukasa, S.B. (2010). Melt extraction and melt refertilization in mantle peridotite of the Coast Range ophiolite: an LA-ICP-MS study. *Contributions to Mineralogy and Petrology* **159**, 113-136

Jochum, K.P., Weis, U., Stoll, B., Kuzmin, D., Yang, Q.C., Raczek, I., Jacob, D.E., Stracke, A., Birbaum, K., Frick, D.A., Gunther, D., Enzweiler, J., (2011). Determination of Reference Values for NIST SRM 610-617 Glasses Following ISO Guidelines. *Geostandards and Geoanalytical Research* **35**, 397-429

Johnson, K.T.M., Dick, H.J.B., Shimizu, N. (1990). Melting in the Oceanic Upper Mantle; An Ion Microprobe Study of Diopsides in Abyssal Peridotites. *Journal of Geophysical Research* **95**, 2661-2678

Kaeser, B., Kalt, A., Pettke, T. (2006). Evolution of the Lithospheric Mantle beneath the Marsabit Volcanic Field (Northern Kenya): Constraints from the Textural, *P-T* and Geochemical Studies on Xenoliths. *Journal of Petrology* **47**, 2149-2184

Kamenov, G.D., Perfit, M.R., Mueller, P.A., Jonasson, I.R. (2008). Controls on magmatism in an island arc environment: study of lavas and sub-arc xenoliths from the Tabar-Lihir-Tanga-Feni island chain, Papua New Guinea. *Contributions to Mineralogy and Petrology* **155**, 635-656

Kelemen, P.B., Dick, H.J.B., Quick, J.E. (1992). Formation of harzburgite by pervasive melt rock reaction in the upper mantle. *Nature* **358**, 635-641

Downloaded from https://academic.oup.com/petrology/article-abstract/doi/10.1093/petrology/egx062/4523818
by University of Durham user
on 07 November 2017

Kepezhinskas, P.K., Defant, M.J., Drummond, M.S. (1995). Na Metasomatism in the Island-Arc Mantle by Slab Melt-Peridotite Interaction: Evidence from Mantle Xenoliths in the North Kamchatka Arc. *Journal of Petrology* **36**, 1505-1527

Klein-BenDavid, O. & Pearson, D.G. (2009). Origins of subcalcic garnets and their relation to diamond-forming fluids-Case studies from Ekati (NWT-Canada) and Murowa (Zimbabwe). *Geochimica et Cosmochimica Acta* **73**, 837-855

Lee, C.T.A., Harbert, A., Leeman, W.P. (2007). Extension of lattice strain theory to mineral/mineral rare-earth element partitioning: An approach for assessing disequilibrium and developing internally consistent partition coefficients between olivine, orthopyroxene, clinopyroxene and basaltic melt. *Geochimica et Cosmochimica Acta* **71**, 481-496

Liang, Y., Sun, C., Yao, L. (2013). A REE-in-two-pyroxene thermometer for mafic and ultramafic rocks. *Geochimica et Cosmochimica Acta* 102, 246-260

Liang, Y. (2014). Time scales of diffusive re-equilibration in bi-mineralic systems with and without a fluid or melt phase. *Geochimica et Cosmochimica Acta* **132**, 274-287

Linckens, J., Herwegh, M., Müntener, O., Mercolli, I. (2011). Evolution of a polymineralic mantle shear zone and the role of second phases in the localisation of deformation. *Journal of Geophysical Research* **116** (B6) DOI: 10.1029/2010JB008119

Mallmann, G. & O'Neill, H.St.C. (2013). Calibration of an Empirical Thermometer and Oxybarometer based on the Partitioning of Sc, Y and V between Olivine and Silicate Melt. *Journal of Petrology* **54**, 933-949

Downloaded from https://academic.oup.com/petrology/article-abstract/doi/10.1093/petrology/egx062/4523818
by University of Durham user
on 07 November 2017

Maury, R.C., Defant, M.J., Joron, J-L. (1992). Metasomatism of the sub-arc mantle inferred from trace elements in Philippine xenoliths. *Nature* **360**, 661-663

McCoy-West, A.J., Bennett, V.C., O'Neill, H.St.C., Hermann, J., Puchtel, I.S. (2015). The Interplay between Melting, Refertilization and Carbonatite Metasomatism in Off-Cratonic Lithospheric Mantle under Zealandia: an Integrated Major, Trace and Platinum Group Element Study. *Journal of Petrology* **56**, 563-604

McDade, P., Blundy, J.D., Wood, B.J. (2003a). Trace element partitioning between mantle wedge peridotite and hydrous MgO-rich melt. *American Mineralogist* **88**, 1825-1831

McDade, P., Blundy, J.D., Wood, B.J. (2003b). Trace element partitioning on the Tinaquillo Lherzolite solidus at 1.5 GPa. *Physics of Earth and Planetary Interiors* **139**, 129-147

McInnes, B.I.A., Grégoire, M., Binns, R.A., Herzig, P.M., Hannington, M.D. (2001). Hydrous metasomatism of oceanic sub-arc mantle, Lihir, Papua New Guinea: petrology and geochemistry of fluid-metasomatised mantle wedge xenoliths. *Earth and Planetary Science Letters* **188**, 169-183

Morgan, Z., Liang, Y., Kelemen, P. (2008). Significance of the concentration gradients associated with dunite bodies in the Josephine and Trinity ophiolites. *Geochemistry, Geophysics, Geosystems* **9**, DOI:10.1029/2008GC001954

Morishita, T., Tani, K., Shukuno, H., Harigane, Y., Tamura, A., Kumagai, H., Hellebrand, E. (2011). Diversity of melt conduits in the Izu-Bonin-Mariana forearc mantle: Implications for the earliest stage of arc magmatism. *Geology* **39**, 411-414

Downloaded from https://academic.oup.com/petrology/article-abstract/doi/10.1093/petrology/egx062/4523818
by University of Durham user
on 07 November 2017

Müller, T., Dohmen, R., Becker, H.W., ter Heege, J.H., Chakraborty, S. (2013). Fe-Mg interdiffusion rates in clinopyroxene: experimental data and implications for Fe-Mg exchange goethermometers. *Contributions to Mineralogy and Petrology* **166**, 1563-1576

Neumann, E-R., Griffin, W.L., Pearson, N.J., O'Reilly, S.Y. (2004). The Evolution of the Upper Mantle beneath the Canary Islands: Information from Trace Elements and Sr isotope Ratios in Minerals in Mantle Xenoliths. *Journal of Petrology* **45**, 2573-2612

O'Neill, H.S. & Wall, V.J. (1987). The Olivine-Orthopyroxene-Spinel Geobarometer, the Nickel Precipitation Curve, and the Oxygen Fugacity of the Earth's Upper Mantle. *Journal of Petrology* **28**, 1169-1191

Olgaard, D.L. & Evans, B. (1986). Effect of second-phase particles on grain growth in calcite. *Journal of the American Ceramic Society* **69**, C272-C277

Palme, H. & O'Neill, H.St.C. (2003). *Cosmochemical Estimates of Mantle Composition*. In: Holland, H.D. & Turekian K.K. (ed.) *Treatise on Geochemistry,* **2** 1-38

Parkinson, I.J. & Pearce, J.A. (1998). Peridotites from the Izu-Bonin-Mariana Forearc (ODP Leg 125): Evidence for Mantle Melting and Melt-Mantle Interaction in a Supra-Subduction Zone Setting. *Journal of Petrology* **39**, 1577-1618

Parkinson, I.J., Hawkesworth, C.J., Cohen, A.S. (1998). Ancient Mantle in a Modern Arc: Osmium Isotopes in Izu-Bonin-Mariana Forearc Peridotites. *Science* **281**, 2011-2013

Parkinson, I.J. & Arculus, R.J. (1999). The redox state of subduction zones: insights from arc-peridotites. *Chemical Geology* **160**, 409-423

Downloaded from https://academic.oup.com/petrology/article-abstract/doi/10.1093/petrology/egx062/4523818
by University of Durham user
on 07 November 2017

Parkinson, I.J., Arculus, R.J., Eggins, S.M. (2003). Peridotite xenoliths from Grenada, Lesser Antilles Island Arc. *Contributions to Mineralogy and Petrology* **146**, 241-262

Parman, S.W., Grove, T.L., Dann, J.C.,de Wit, M.J. (2004). A subduction origin for komatiites and cratonic lithospheric mantle. *South African Journal of Geology* **107**, 107-118

Pearce, J.A., Barker, P.F., Edwards, S.J., Parkinson, I.J., Leat, P.T. (2000). Geochemistry and tectonic significance of peridotites from the South Sandwich arc-basin system, South Atlantic. *Contributions to Mineralogy and Petrology* **139**, 36-53

Pearson, D.G. & Canil, D., Shirey, S.B. (2003). *Mantle Samples Included in Volcanic Rocks: Xenoliths and Diamonds.* In: Holland, H.D. & Turekian K.K. (ed.) *Treatise on Geochemistry,* **2** 171-275

Pearson D.G. & Wittig, N. (2008). Formation of Archaean continental lithosphere and its diamonds: the root of the problem. *Journal of the Geological Society* **165**, 895-914

Pirard, C., Hermann, J., O'Neill, H.St.C. (2013). Petrology and Geochemistry of the Crust-Mantle Boundary in a Nascent Arc, Massif du Sud Ophiolite, New Caledonia, SW Pacific. *Journal of Petrology* **54**, 1759-1792

Pirard, C. & Hermann, J. (2015). Focused fluid transfer through the mantle above subduction zones. *Geology* **43**, 915-918

Plank, T. & Langmuir, C.H. (1993). Tracing trace-elements from sediment input to volcanic output at subduction zones. *Nature* **362**, 739-743

Downloaded from https://academic.oup.com/petrology/article-abstract/doi/10.1093/petrology/egx062/4523818
by University of Durham user
on 07 November 2017

Schiano, P., Bourdon, B. (1999). On the preservation of mantle information in ultramafic nodules: glass inclusions within minerals versus interstitial glasses. *Earth and Planetary Science Letters* **169**, 173-188

Scambelluri, M., Hermann, J., Morten, L., Rampone, E. (2006). Melt- versus fluid-induced metasomatism in spinel to garnet wedge peridotites (Ulten Zone, Eastern Italian Alps): clues from trace element and Li abundances. *Contributions to Mineralogy and Petrology* **151**, 372-394

Seyler, M., Cannat, M., Mével, C. (2003). Evidence for major-element heterogeneity in the mantle source of abyssal peridotites from the Southwest Indian Ridge (52° to 68°E). *Geochemistry, Geophysics, Geosystems* **4**, doi:10.1029/2002GC000305

Seyler, M., Brunelli, D., Toplis, M.J., Mével, C. (2011). Multiscale chemical heterogeneities beneath the eastern Southwest Indian Ridge (52°E-68°E): Trace element compositions of along-axis dredged peridotites. *Geochemistry, Geophysics, Geosystems* **12**, doi:10.1029/2011GC003585

Shaw, C.S.J. (2009). Textural development of amphibole during breakdown reactions in a synthetic peridotite. *Lithos* **110**, 215-228

Shaw, C.S.J., Dingwell, D.B. (2008). Experimental peridotite-melt reaction at one atmosphere: a textural and chemical study. *Contributions to Mineralogy and Petrology* **155**, 199-214

Simon, N.S.C., Carlson, R.W., Pearson, D.G., Davies, G.R. (2007). The Origin and Evolution of the Kaapvaal Cratonic Lithospheric Mantle. *Journal of Petrology* **48**, 589-625

Downloaded from https://academic.oup.com/petrology/article-abstract/doi/10.1093/petrology/egx062/4523818
by University of Durham user
on 07 November 2017

Smith, D., Riter, J.C.A., Mertzman, S.A. (1999). Water-rock interactions, orthopyroxene growth, and Si-enrichment in the mantle: evidence in the xenoliths from the Colorado Plateau, south-western United States. *Earth and Planetary Science Letters* **165**, 45-54

Smith, D. (2013). Olivine thermometry and source constraints for mantle fragments in the Navajo Volcanic Field, Colorado Plateau, southwest United States: Implications for the Mantle Wedge. *Geochemistry, Geophysics, Geosystems* **14** doi:10.1002/ggge.20065

Spandler, C. & O'Neill, H.St.C. (2010). Diffusion and partition coefficients of minor and trace elements in San Carlos olivine at 1,300 °C with some geochemical implications. *Contributions to Mineralogy and Petrology* **159**, 791-818

Stachel, T., Viljoen, K.S., Brey, G., Harris, J.W. (1998). Metasomatic processes in lherzolitic and harzburgitic domains of diamondiferous lithospheric mantle: REE in garnets from xenoliths and inclusions in diamonds. *Earth and Planetary Science Letters* **159**, 1-12

Stachel, T., Aulbach, S., Brey, G.P., Harris, J.W., Leost, I., Tappert, R., Viljoen, K.S. (2004). The trace element composition of silicate inclusions in diamonds: a review. *Lithos* **77**, 1-19

Suhr, G., Hellebrand, E., Snow, J.E., Seck, H.A., Hofmann, A.W. (2003). Significance of large, refractory dunite bodies in the upper mantle of the Bay of Islands Ophiolite. *Geochemistry, Geophysics, Geosystems* **4**, doi:10.1029/2008GC002012

Sun, C. & Liang, Y. (2013). The importance of crystal chemistry on REE partitioning between mantle minerals (garnet, clinopyroxene, orthopyroxene, and olivine) and basaltic melts. *Chemical Geology* **358**, 23-36

Downloaded from https://academic.oup.com/petrology/article-abstract/doi/10.1093/petrology/egx062/4523818
by University of Durham user
on 07 November 2017

Sun, C. & Liang, Y. (2014). An assessment of subsolidus re-equilibration on REE distribution among mantle minerals olivine, orthpyroxene, clinopyroxene, and garnet in peridotites. *Chemical Geology* **372**, 80-91

Tappe, S., Smart, K.A., Pearson, D.G., Steenfelt, A., Simonetti, A. (2011). Craton formation in Late Archean subduction zones revealed by first Greenland eclogites. *Geology* **39**, 1103-1106

Tamura, Y., Ishizuka, O., Stern, R.J., Nichols, A.R.L., Kawabata, H., Hirahara, Y., Chang, Q., Miyazaki, T., Kimura, J.I., Embley, R.W., Tatsumi, Y. (2014). Mission Immiscible: Distinct Subduction Components Generate Two Primary Magmas at Pagan Volcano, Mariana Arc. *Journal of Petrology* **55**, 63-101

Tollan, P.M.E., O'Neill, H.St.C., Hermann, J., Benedictus, A., Arculus, R.J. (2015). Frozen melt-rock reaction in a peridotite xenolith from sub-arc mantle recorded by diffusion of trace elements and water in olivine. *Earth and Planetary Science Letters* **422**, 169-181

Turner, S., Caulfield, J., Turner, M., van Keken, P., Maury, R., Sandiford, M., Prouteau, G. (2012). Recent contribution of sediments and fluids to the mantle's volatile budget. *Nature Geoscience* **5**, 50-54

Tursack, E. & Liang, Y. (2012). A comparative study of melt-rock reactions in the mantle: laboratory dissolution experiments and geological field observations. *Contributions to Mineralogy and Petrology* **163**, 861-876

Vannucci, R., Tiepolo, M., Defant, M.J., Kepezhinskas, P. (2007). The metasomatic record in the shallow peridotite mantle beneath Grenada (Lesser Antilles arc). *Lithos* **99**, 25-44

Downloaded from https://academic.oup.com/petrology/article-abstract/doi/10.1093/petrology/egx062/4523818
by University of Durham user
on 07 November 2017

Van Orman, J.A., Grove, T.L., Shimizu, N. (2001). Rare earth element diffusion in diopside: influence of temperature, pressure, and ionic radius, and an elastic model for diffusion in silicates. *Contributions to Mineralogy and Petrology* **141**, 687-703

Voigt, M., von der Handt, A., (2011). Influence of subsolidus processes on the chromium number in spinel in ultramafic rocks. *Contributions to Mineralogy and Petrology* **162**, 675-689

Ward, S.N., Day, S., (2003). Ritter Island Volcano- lateral collapse and the tsunami of 1888. *Geophysical Journal International* **154**, 891-902

Warren, J.M., Shimizu, N., Sakaguchi, C., Dick, H.J.B., Nakamura, E. (2009). An assessment of upper mantle heterogeneity based on abyssal peridotite isotopic compositions. *Journal of Geophysical Research* **114**, doi:10.1029/2008JB006186

Widom, E., Kepezhinskas, P., Defant, M. (2003). The nature of metasomatism in the sub-arc mantle wedge: evidence from Re-Os isotopes in Kamchatka peridotite xenoliths. *Chemical Geology* **196**, 283-306

Witt-Eickschen, G. & O'Neill, H.St.C. (2005). The effect of temperature on the equilibrium distribution of trace elements between clinopyroxene, orthopyroxene, olivine and spinel in upper mantle peridotite. *Chemical Geology* **221**, 65-101

Witt-Eickschen, G., Palme, H., O'Neill, H.S.C., Allen, C.M., (2009). The geochemistry of the volatile trace elements As, Cd, Ga, In and Sn in the Earth's mantle: New evidence from in situ analyses of mantle xenoliths. *Geochimica et Cosmochimia Acta* **73**, 1755-1778

Downloaded from https://academic.oup.com/petrology/article-abstract/doi/10.1093/petrology/egx062/4523818
by University of Durham user
on 07 November 2017

Woodhead, J.D., Eggins, S.M., Johnson, R.W. (1998). Magma Genesis in the New Britain Island Arc: Further Insights into Melting and Mass Transfer Processes. *Journal of Petrology* **39**, 1641-1668

Woodhead, J., Hergt, J., Sandiford, M., Johnson, W. (2010). The big crunch: Physical and chemical expressions of arc/continent collision in the Western Bismarck arc. *Journal of Volcanology and Geothermal Research* **190**, 11-24

Zheng, J.P., Zhang, R.Y., Griffin, W.L., Liou, J.G., O'Reilly, S.Y. (2005). Heterogeneous and metasomatized mantle recorded by trace elements in minerals of the Donghai garnet peridotites, Sulu UHP terrane, China. *Chemical Geology* **221**, 243-259

Zheng, J.P., Griffin, W.L., O'Reilly, S.Y., Yu, C.M., Zhang, H.F., Pearson, N., Zhang, M. (2007). Mechanism and timing of lithospheric modification and replacement beneath the eastern North China Craton: Peridotitic xenoliths from the 100 Ma Fuxin basalts and a regional synthesis. *Geochimica et Cosmochimica Acta* **71**, 5203-5225

Zou, H. (1998). Trace element fractionation during modal and nonmodal dynamic melting and open-system melting: A mathematical treatment. *Geochimica et Cosmochimica Acta* **62**, 1937-1945

FIGURE AND TABLE CAPTIONS

Fig. 1 Map from Tollan *et al.* (2015) showing the Bismarck archipelago and the location of key islands, including Ritter. The West Bismarck island arc extends westwards from the western-most point of New Britain. Inset map shows in more detail Ritter Island, the surrounding ocean

Downloaded from https://academic.oup.com/petrology/article-abstract/doi/10.1093/petrology/egx062/4523818
by University of Durham user
on 07 November 2017

bathymetry and the locations of dredged cones. Only samples from Cone 4 are studied here. Map adapted from Ward & Day (2003)

Fig. 2 Thin section photomicrographs (cross polarised light) of Ritter peridotites. (a) and (b) display typical coarse, well-equilibrated textures of 'residual' peridotites. (c) to (f) show the formation of secondary orthopyroxene through reaction between olivine and silicate melt

Fig. 3 Scanning electron microscope images of reaction textures in Ritter peridotites. (a) 67-02A(5): large circular holes are LA-ICP-MS spots. (b) 67-02B(5). (c) 67-02B(3): note the absence of interstitial glass or cpx in the opx vein. (d) 67-02D(4). (e) 67-02D(7): large circular hole is an LA-ICP-MS spot.

Fig. 4 Co-variation of mineral major element compositions for Ritter peridotites, compared to representative literature data for cratonic (Bernstein *et al.,* 2006), arc (Parkinson & Pearce, 1998; Ionov, 2010) and abyssal (Seyler *et al.,* 2003) peridotites. Data presented are averages for each sample. Inset in (a) shows the complete dataset for dunitic and peridotitic olivine.

Fig. 5 Olivine and spinel compositions from the Ritter peridotites and dunites compared to the olivine-spinel-mantle-array (OSMA) of Arai (1994). Ritter peridotites are separated into those containing reaction textures and those containing only protogranular textures. Note, the four peridotite samples with the highest spinel Cr# all uniquely contain glass in their reaction patches.

Fig. 6 Representative trace element concentrations in orthopyroxenes from the Ritter peridotites, normalised to primitive mantle (Palme & O'Neill, 2003). Left panels are normalised REE patterns, right panels are normalised extended trace element patterns for the same samples. Each sample displays analyses of multiple crystals. The shaded grey fields represent abyssal peridotite data (Warren *et al.,* 2009; Seyler *et al.,* 2011)

Downloaded from https://academic.oup.com/petrology/article-abstract/doi/10.1093/petrology/egx062/4523818
by University of Durham user
on 07 November 2017

Fig. 7 (a-c) Comparison between analyses of residual opx and secondary opx/reaction patches in samples 67-02D(4), 67-02A(5) and 67-02B(3) (from top to bottom). (d-f) Differences in ratios of similarly compatible, but anomalously behaving, elements in residual opx and secondary opx/reaction patches. Data for all samples are displayed in each subplot. Average values are reported in the Supplementary Data.

Fig. 8 Representative trace element concentrations of clinopyroxene from the Ritter peridotites (a, b), and pyroxenites (c, d) normalised to primitive mantle (Palme & O'Neill, 2003). Left panels are normalised REE patterns, right panels are normalised extended trace element patterns for the same samples. The different clinopyroxene populations (Type I, II and III) are plotted with different symbols for clarity. Each pattern represents a different sample, and is the average of 2-5 crystals.

Fig. 9 Variation in the trace element compositions of multiple olivines from different peridotite samples. Peridotite samples are separated into those containing reaction textures and those only containing protogranular textures, to illustrate chemical differences in the olivines. The concentrations are compared with the global mantle olivine array; data from Grégoire *et al.,* 2001; Neumann *et al.,* 2004; Witt-Eickschen & O'Neill, 2005; Zheng *et al.,* 2005; Kaeser *et al.,* 2006; Zheng *et al.,* 2007; De Hoog *et al.,* 2010; Batanova *et al.,* 2011; Ionov, 2010; Pirard *et al.,* 2013; Smith, 2013.

Fig. 10 Simple chronology progressing from left to right (oldest to youngest) showing the appearance and disappearance of phases as a function of major petrological stages: Stage 1, partial melting; Stage 2, cpx metasomatism and pyroxenite/dunite formation; Stage 3, cooling; Stage 4, melt-rock reaction; Stage 5, exhumation. Phases are grouped as follows: A, residual

Downloaded from https://academic.oup.com/petrology/article-abstract/doi/10.1093/petrology/egx062/4523818
by University of Durham user
on 07 November 2017

phases; B, secondary cpx; C, reaction patches and secondary opx; D, pyroxenites and dunites. Dashed lines indicate partial retention/alteration of phase. The upper panel schematically shows changing temperature (^{o}C) with time.

Fig. 11 Results of isothermal, isobaric fractional melting modelling of a depleted mantle source under hydrous and anhydrous conditions for Y and Yb in residual orthopyroxene. Each data point represents a single crystal analysis (instead of sample averages). Pale coloured data points reflect a correction for trace element exchange during sub-solidus cooling between clinopyroxene and orthopyroxene and, after clinopyroxene exhaustion, between orthopyroxene and olivine. Whilst anhydrous melting up to clinopyroxene-out can explain abyssal peridotites, the highly depleted trace element concentrations of orthopyroxene require a hydrous melting scenario. Sub-solidus cooling has little effect on the concentrations of Y and Yb in orthopyroxene. See text for full details. Abyssal peridotite data are from Hellebrand *et al.* (2005); Warren *et al.* (2009); Brunelli & Seyler (2010) and Seyler *et al.* (2011).

Fig. 12 (a) Correlation between temperature calculated by Fe-Mg exchange between olivine and spinel (O'Neill & Wall, 1987) and by major component exchange between clinopyroxene and orthopyroxene (Brey & Kohler, 1990) for the Ritter peridotites. Samples are separated into those containing reaction textures and those only containing protogranular textures. Note that two samples which contain localised reaction patches composed of fine, inter-mixed orthopyroxene and clinopyroxene have significantly higher two-pyroxene temperatures which are not plotted (Table 7). (b) Temperatures calculated from Fe-Mg exchange between olivine and spinel (O'Neill & Wall, 1987; ONW), Al exchange between olivine and spinel (Wan *et al.,* 2008; WCC), Al in olivine (De Hoog *et al.,* 2010; DHGC), major component exchange between two

Downloaded from https://academic.oup.com/petrology/article-abstract/doi/10.1093/petrology/egx062/4523818
by University of Durham user
on 07 November 2017

pyroxenes (Brey & Kohler, 1990; BK), Ca in orthopyroxene (Brey & Kohler, 1990; BK) and REE exchange between two pyroxenes (Liang *et al.,* 2013; LSY)

Fig. 13 Trace element exchange between: (a) and (b) clinopyroxene and olivine; (c) and (d) clinopyroxene and orthopyroxene; (e) and (f) orthopyroxene and olivine. Data are plotted *versus* temperature calculated from olivine-spinel Fe-Mg exchange (O'Neill & Wall, 1987) and compared to global data for well equilibrated peridotites and experiments.

Fig. 14 (a) Temperatures calculated for texturally equilibrated Ritter peridotites using a range of geothermometers (O'Neill & Wall, 1987; Brey & Kohler, 1990; Liang *et al.,* 2013) vs. the diffusivity (D_0) of the major component involved in the exchange reaction. Diffusivity of Fe-Mg in olivine from Dohmen & Chakraborty (2007), Fe-Mg in cpx from Müller *et al.* (2013) and Ce and Yb in cpx from Van Orman *et al.* (2001). Dashed and dotted lines represent the effects of different cooling rates on closure temperatures. Best fit result for a grain radius of 2 mm gives a cooling rate of 20 ºC/Ma. **(b)** Comparison of thermometry results for well-equilibrated peridotites from this study with data for abyssal peridotites, mid-ocean ridge (MOR) ophiolites and supra-subduction zone (SSZ) ophiolites from Dygert & Liang (2015). Numbers on vertical tie lines are cooling rates in ºC/Ma calculated by Dygert & Liang (2015). The figure is adapted from Fig. 9b of Dygert & Liang (2015). Red lines represent cooling paths from different initial temperatures. BKN is the 2-pyroxene thermometer of Brey & Kohler (1990) and LSY is the 2-pyroxene REE exchange thermometer of Liang *et al.* (2013).

Fig. 15 Results of models calculating how the concentrations of Y and Yb in clinopyroxene, orthopyroxene and olivine would change during sub-solidus cooling relative to their initial

Downloaded from https://academic.oup.com/petrology/article-abstract/doi/10.1093/petrology/egx062/4523818
by University of Durham user
on 07 November 2017

concentrations. The model assumes a constant harzburgitic mineralogy of 74 % olivine, 25 % orthopyroxene and 1 % clinopyroxene.

Fig. 16 Summary of the petrological evolution of the Ritter peridotites. (a) This involves melting and metasomatism by multiple slab-derived fluids as part of an 'ancient' arc systems (b) a period of cooling to low ambient mantle temperatures followed by melt-rock reaction in the upper mantle wedge as part of the modern West Bismarck arc. See text for full details.

Downloaded from https://academic.oup.com/petrology/article-abstract/doi/10.1093/petrology/egx062/4523818
by University of Durham user
on 07 November 2017

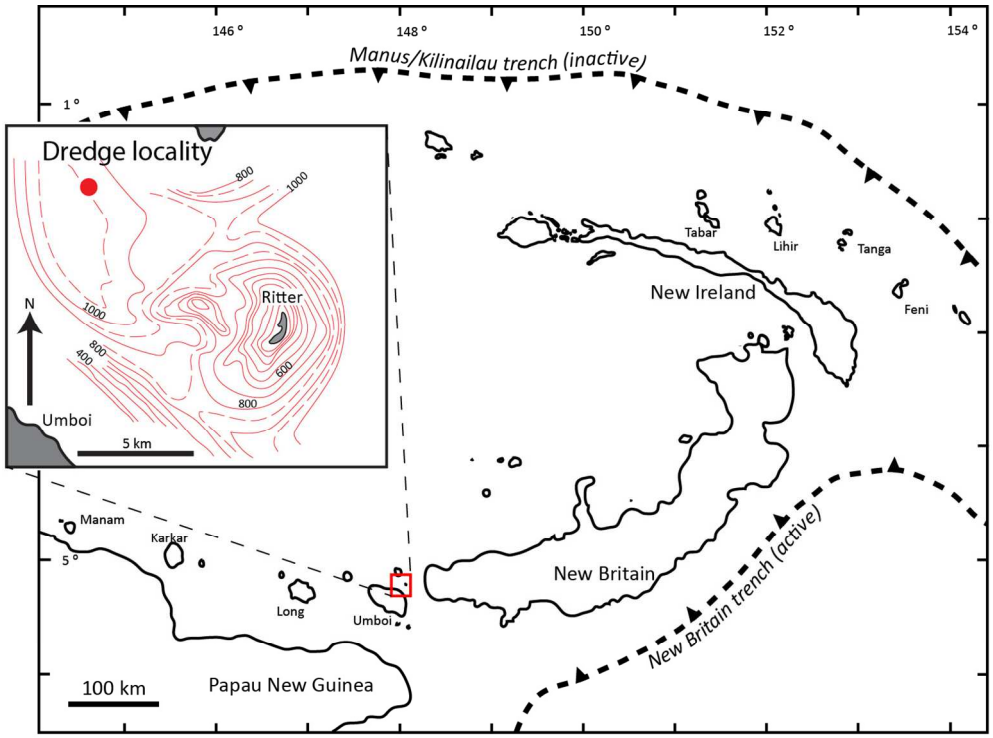

Fig. 1

130x96mm (300 x 300 DPI)

Downloaded from https://academic.oup.com/petrology/article-abstract/doi/10.1093/petrology/egx062/4523818
by University of Durham user
on 07 November 2017

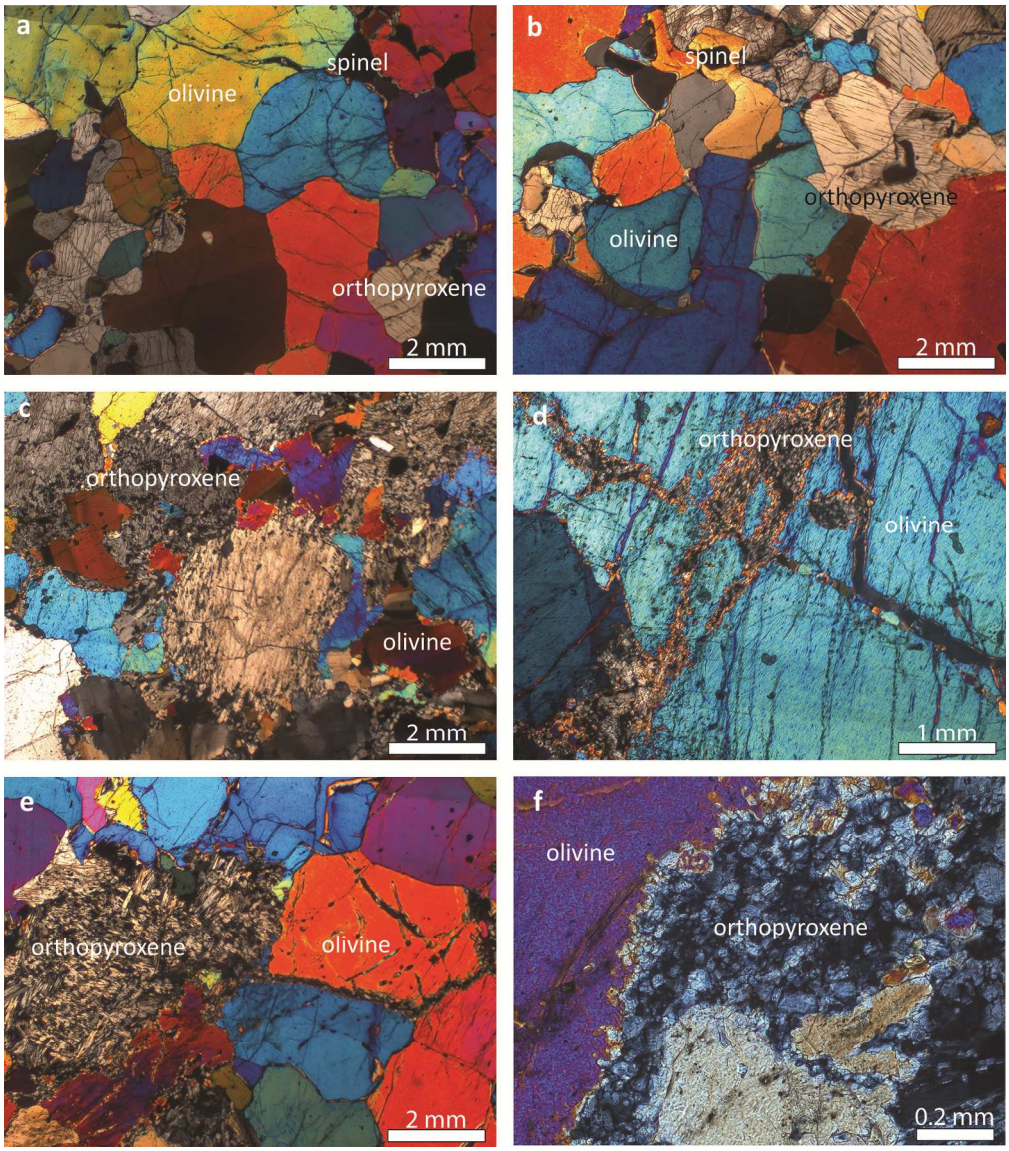

Fig. 2

164x187mm (300 x 300 DPI)

Downloaded from https://academic.oup.com/petrology/article-abstract/doi/10.1093/petrology/egx062/4523818
by University of Durham user
on 07 November 2017

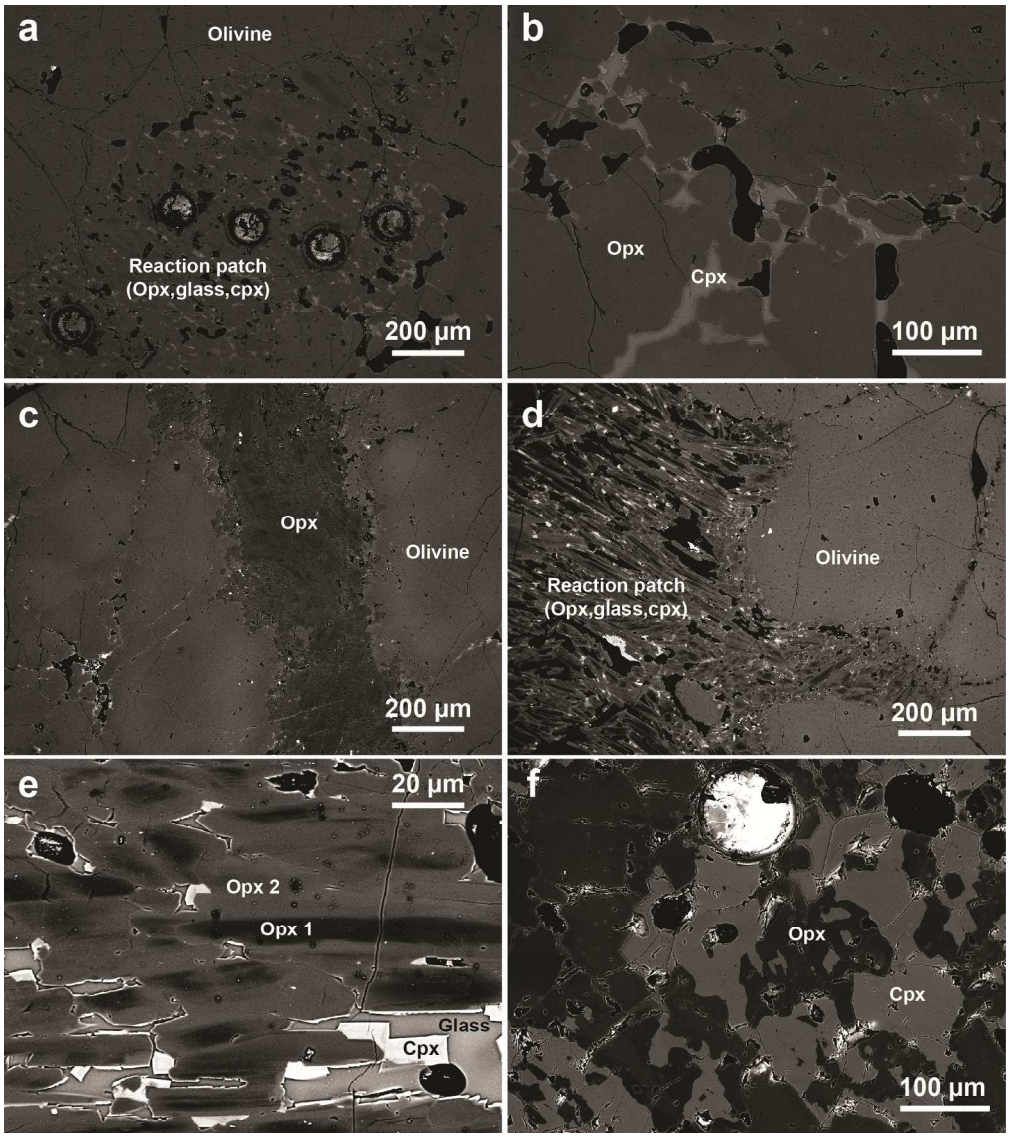

Fig. 3

182x205mm (300 x 300 DPI)

Downloaded from https://academic.oup.com/petrology/article-abstract/doi/10.1093/petrology/egx062/4523818
by University of Durham user
on 07 November 2017

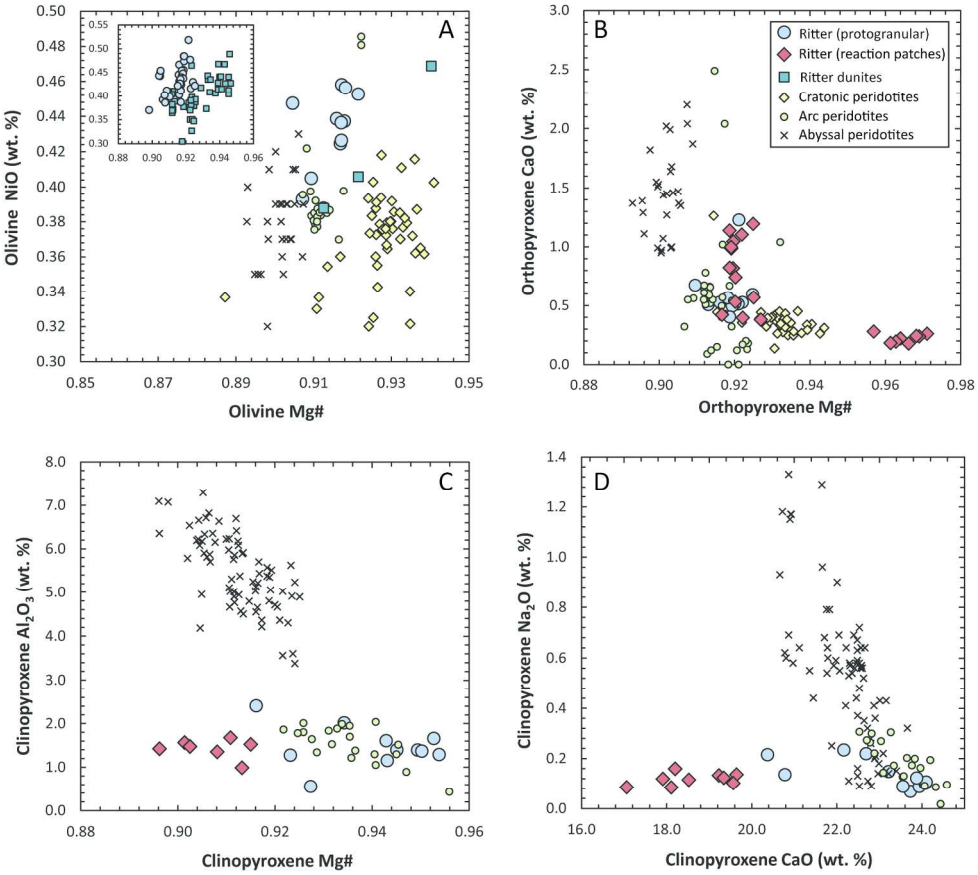

Fig. 4

188x167mm (300 x 300 DPI)

Downloaded from https://academic.oup.com/petrology/article-abstract/doi/10.1093/petrology/egx062/4523818
by University of Durham user
on 07 November 2017

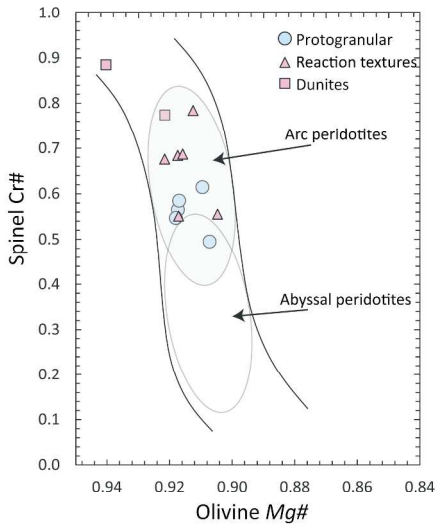

Fig. 5

210x297mm (300 x 300 DPI)

Downloaded from https://academic.oup.com/petrology/article-abstract/doi/10.1093/petrology/egx062/4523818
by University of Durham user
on 07 November 2017

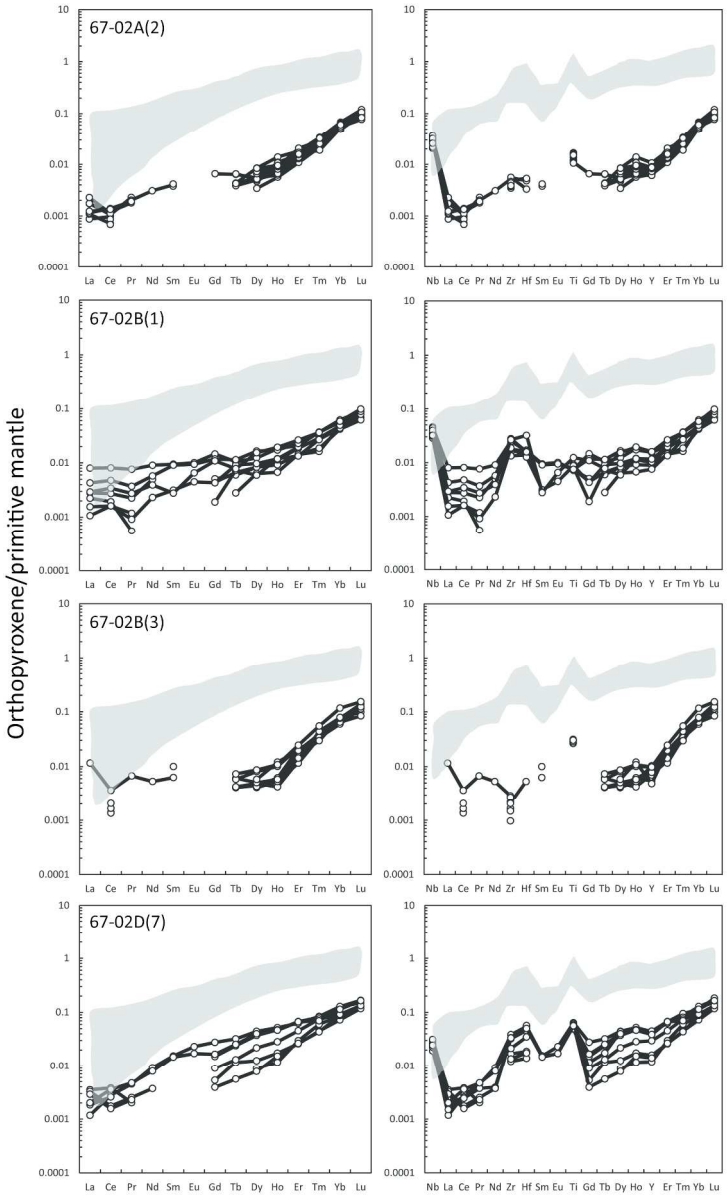

Fig. 6

163x269mm (300 x 300 DPI)

Downloaded from https://academic.oup.com/petrology/article-abstract/doi/10.1093/petrology/egx062/4523818
by University of Durham user
on 07 November 2017

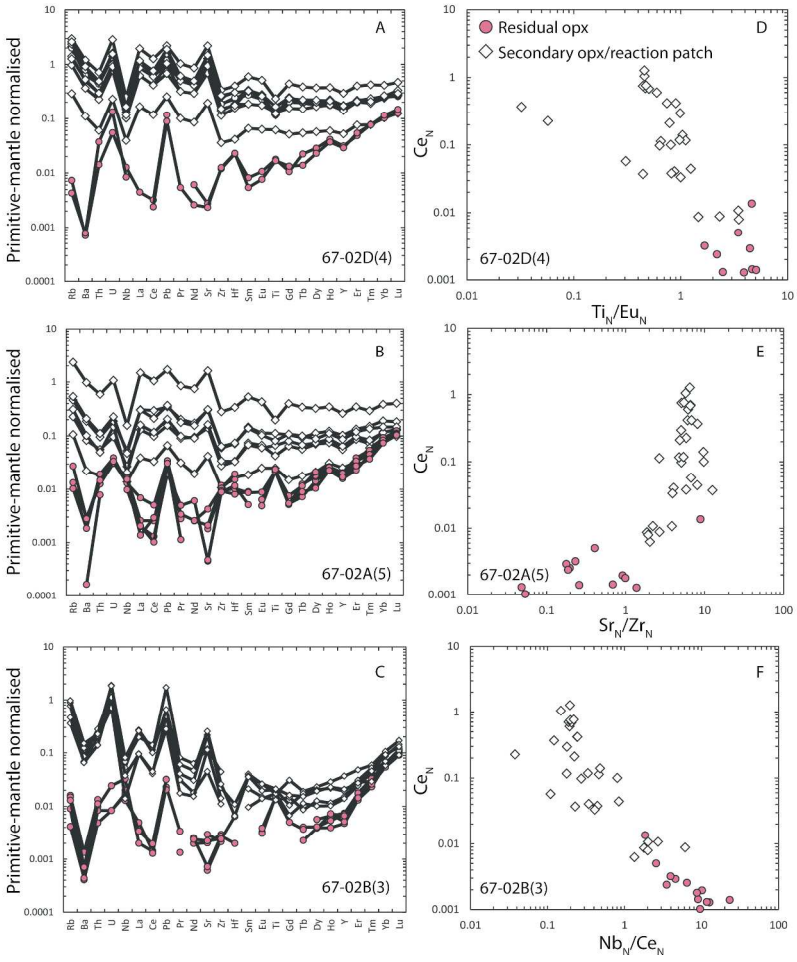

Fig. 7

210x297mm (300 x 300 DPI)

Downloaded from https://academic.oup.com/petrology/article-abstract/doi/10.1093/petrology/egx062/4523818
by University of Durham user
on 07 November 2017

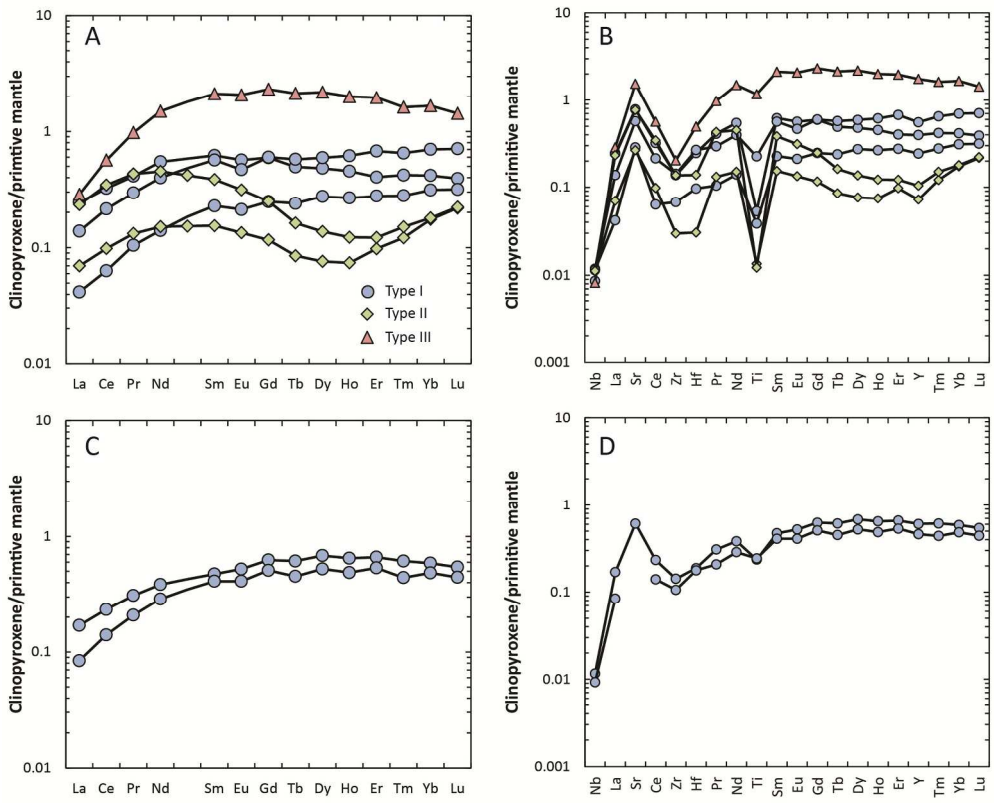

Fig. 8

199x161mm (300 x 300 DPI)

Downloaded from https://academic.oup.com/petrology/article-abstract/doi/10.1093/petrology/egx062/4523818
by University of Durham user
on 07 November 2017

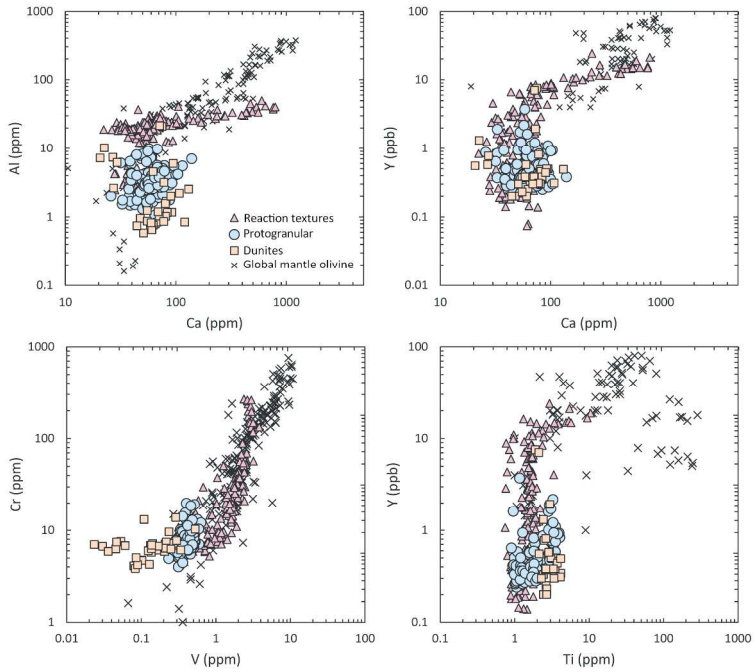

Fig. 9

210x297mm (300 x 300 DPI)

Downloaded from https://academic.oup.com/petrology/article-abstract/doi/10.1093/petrology/egx062/4523818
by University of Durham user
on 07 November 2017

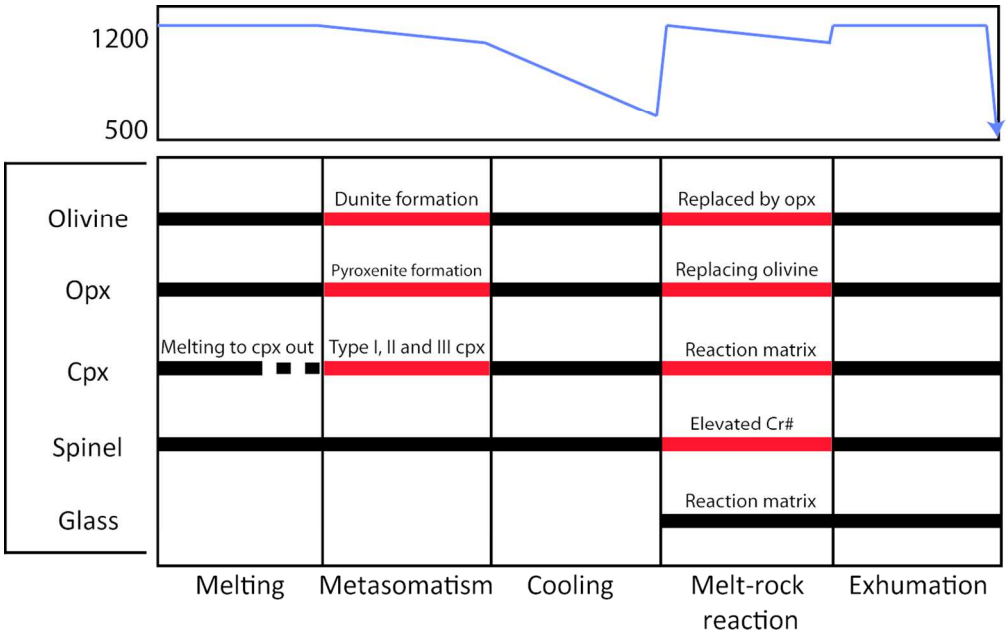

Fig. 10

123x77mm (300 x 300 DPI)

Downloaded from https://academic.oup.com/petrology/article-abstract/doi/10.1093/petrology/egx062/4523818
by University of Durham user
on 07 November 2017

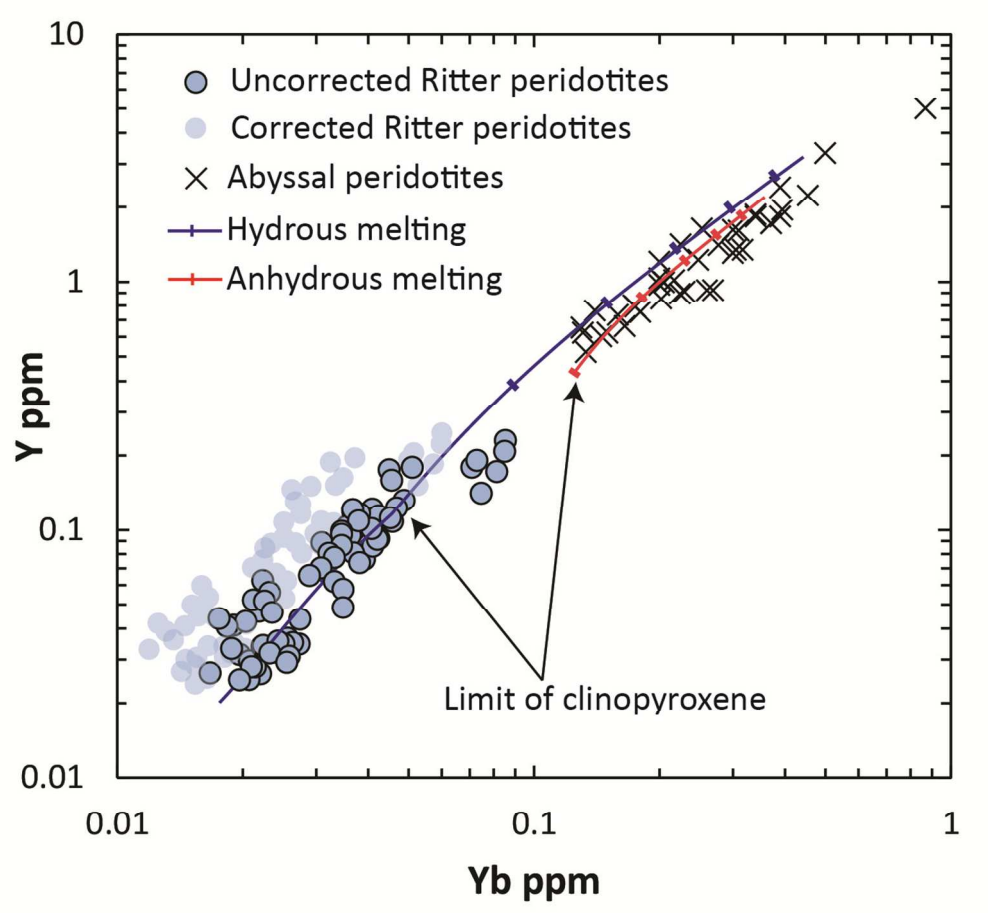

Fig. 11

117x107mm (300 x 300 DPI)

Downloaded from https://academic.oup.com/petrology/article-abstract/doi/10.1093/petrology/egx062/4523818
by University of Durham user
on 07 November 2017

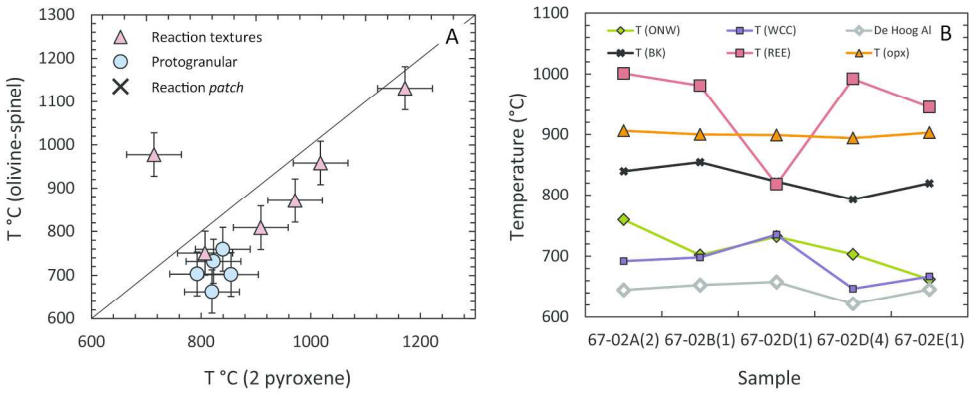

Fig. 12

206x83mm (300 x 300 DPI)

Downloaded from https://academic.oup.com/petrology/article-abstract/doi/10.1093/petrology/egx062/4523818
by University of Durham user
on 07 November 2017

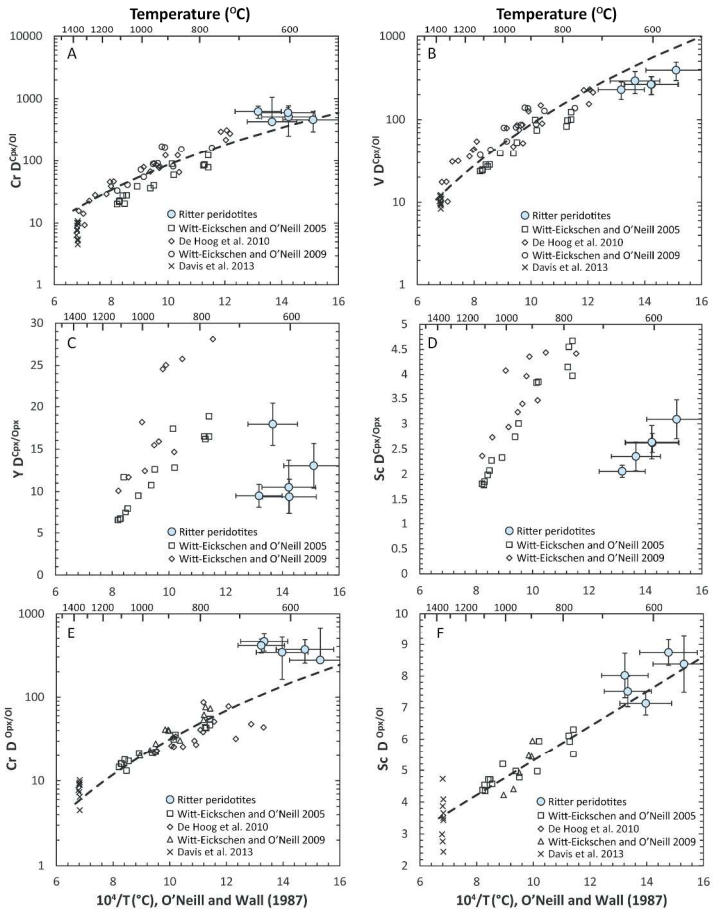

Fig. 13

210x297mm (300 x 300 DPI)

Downloaded from https://academic.oup.com/petrology/article-abstract/doi/10.1093/petrology/egx062/4523818
by University of Durham user
on 07 November 2017

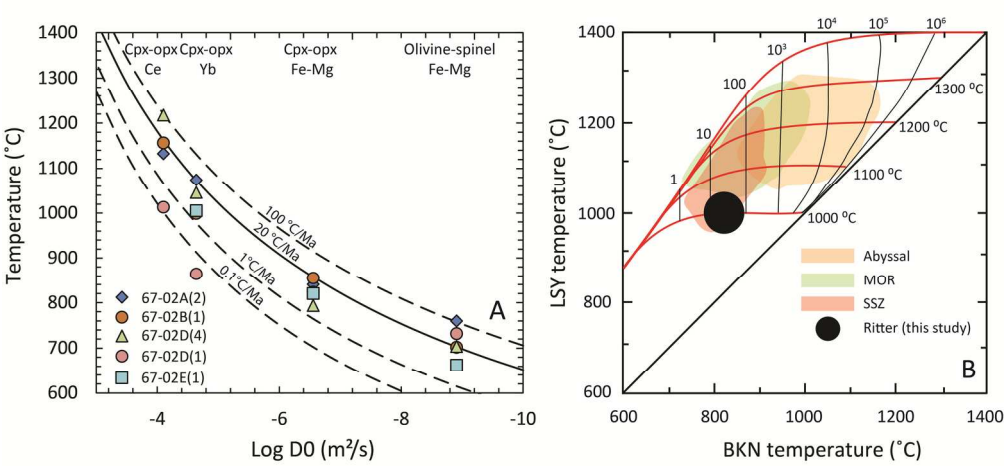

Fig. 14

91x42mm (600 x 600 DPI)

Downloaded from https://academic.oup.com/petrology/article-abstract/doi/10.1093/petrology/egx062/4523818
by University of Durham user
on 07 November 2017

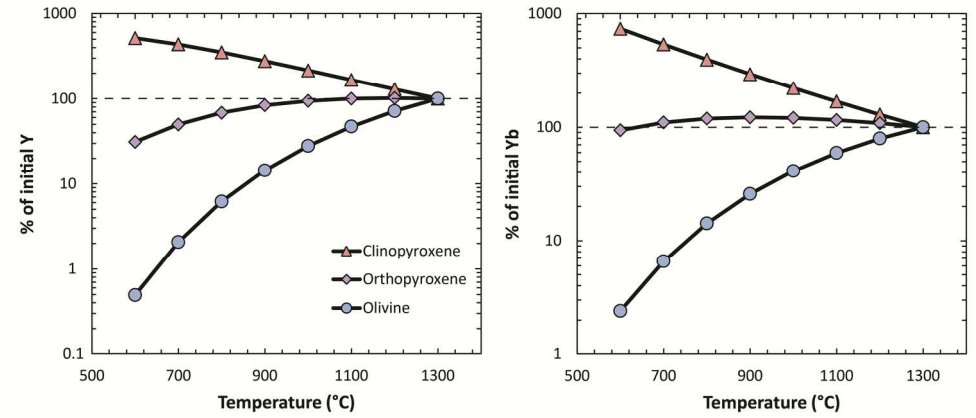

Fig. 15

89x38mm (600 x 600 DPI)

Downloaded from https://academic.oup.com/petrology/article-abstract/doi/10.1093/petrology/egx062/4523818
by University of Durham user
on 07 November 2017

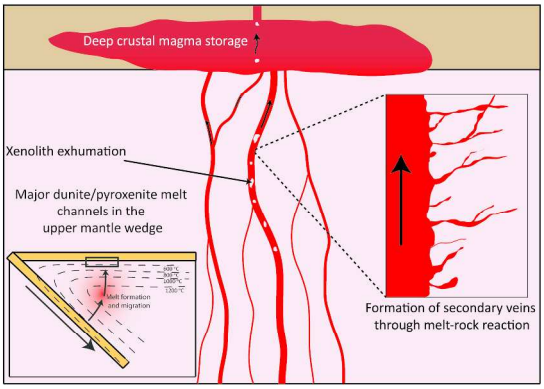

Fig. 16

210x297mm (300 x 300 DPI)

Downloaded from https://academic.oup.com/petrology/article-abstract/doi/10.1093/petrology/egx062/4523818
by University of Durham user
on 07 November 2017

Table 1 Summary of petrographic observations of Ritter samples. ol = olivine, opx = orthopyroxene, cpx = clinopyroxene, sp = spinel. Subscript numbers refer to different populations, explained in the discussion. Cpx_{int} refers to clinopyroxene interstitial to glass and orthopyroxene in reaction patches

			Primary phases			Secondary phases					
Sample	Classification	Description	Ol_1	Opx_1	Ol_2	Opx_2	Cpx_1	Cpx_2	Cpx3	Cpx_{fine}	Glass
67-02A(1)	Pyroxenite	Dominated by opx, with subordinate cpx and sp. 1-2 sets of exsolution lamellae in opx				X	X				
67-02A(2)	Harzburgite	Coarser crystals than other harzburgites. Undulose extinction in ol and exsolution lamellae in opx, typical of 'residual' samples. Sp has dark red core and very thin black rim. Coarse ol are heavily fractured	X	X				X			
67-02A(3)	Dunite/harzburgite	Porphyroclastic texture. Ol porphyroclasts have been partially recrystallised to neoblasts. Sp (black) and opx both show reaction textures. Precipitation of secondary fine grained cpx	X	X	X		X				
67-02A(5)	Harzburgite	Many fibrous opx veins, some patches of fibrous and equant opx with interstitial cpx and glass. Opx veins often cutting ol. Numerous inclusions in opx	X	X		X				X	X
67-02B(1)	Harzburgite	Undulose extinction in ol and opx, but no evidence for reaction with melt other than thin black rim around red core of sp	X	X				X			
67-02B(2)	Dunite	Very coarse ol crystals with large clusters of similarly coarse sp. Traces of melt often surround grain boundaries and fractures	X								
67-02B(3)	Harzburgite	Many fibrous opx veins, often with relic ol within. Thin rims on olivine where close to opx veins. No glass/cpx associated with reaction patches	X	X		X					
67-02B(5)	Harzburgite	Numerous coarse ol and opx with reacted crystal edges, but lacks abundant opx veins. Glass around secondary opx boundaries	X	X		X				X	X
67-02B(6)	Pyroxenite	Two layers. One dominantly opx but with cpx occuring regularly at grain boundaries. 2nd layer is clinopyroxenite. Sp common throughout and contains numerous melt inclusions				X	X				X
67-02D(1)	Harzburgite	Similar textures to other 'residual' peridotites	X	X			X				
67-02D(3)	Dunite	Coarse dunite cross-cut by vein of finer grained ol with intermixed, fine sp. Well equilibrated grain boundaries between primary and secondary dunites	X		X						

Downloaded from https://academic.oup.com/petrology/article-abstract/doi/10.1093/petrology/egx062/4523818
by University of Durham user
on 07 November 2017

67-02D(4)	Harzburgite	Thick section typical of 'residual' peridotites. Thin section shows occasional reaction patches. Coarse relic opx shows evidence for recrystallisation at rims. Reaction patches have a distinct foliation, and are particularly rich in glass and cpx	X	X	X	X		X	X
67-02D(7)	Harzburgite	No secondary opx present, but grain boundaries to all grains are distorted and not in equilibrium with traces of glass present	X	X			X		X
67-02E(1)	Harzburgite	Similar to 67-02B(1). No evidence for reaction with a melt from thin section, however thick section shows a thin vein of cpx	X	X		X			
67-02E(3)	Harzburgite	Numerous veins and patches of secondary opx and cpx. Secondary phases are slightly coarser than other samples and are not accompanied by intserstitial glass	X	X	X			X	

Downloaded from https://academic.oup.com/petrology/article-abstract/doi/10.1093/petrology/egx062/4523818
by University of Durham user
on 07 November 2017

Table 2 Average major element compositions (wt %) of olivine, spinel, orthopyroxene and clinopyroxene in the Ritter samples with a protogranular texture. Mg# = Mg/Mg+Fe, Cr# = Cr/Cr+Al. Fe_2O_3 in spinel was calculated assuming ideal stoichiometry on a 3 cation basis. P = Pyroxenite, D = Dunite, H = Harzburgite

Olivine

	67-02A(1)	67-02B(6)	67-02B(2)		67-02D(3)	67-02A(2)	67-02B(1)	67-02D(1)	67-02D(4)	67-02E(1)	67-02A(3)	67-02A(5)	67-02B(3)	67-02B(5)	67-02D(7)	67-02E(3)
	P	P	D	D	D	H	H	H	H	H	H	H	H	H	H	H
SiO_2			41.58	40.86	39.84	40.90	40.72	40.62	40.62	41.06	40.85	40.16	40.79	41.08	40.53	40.15
TiO_2			<0.05	<0.05	<0.05	<0.05	<0.05	<0.05	<0.05	<0.05	<0.05	<0.05	<0.05	<0.05	<0.05	<0.05
Al_2O_3			<0.04	<0.04	<0.04	<0.04	<0.04	<0.04	<0.04	<0.04	<0.04	<0.04	<0.04	<0.04	<0.04	<0.04
Cr_2O_3			<0.06	0.07	<0.06	<0.06	<0.06	<0.06	<0.06	<0.06	<0.06	<0.06	<0.06	<0.06	<0.06	<0.06
FeO			6.00	8.20	7.72	8.15	8.05	8.21	8.96	9.04	8.63	8.25	8.27	8.21	7.74	9.36
MnO			0.12	0.15	0.08	0.11	0.13	0.11	0.13	0.13	0.13	0.13	0.14	0.15	0.12	0.17
MgO			53.05	49.98	50.82	50.67	50.53	50.81	50.48	49.56	50.55	50.41	51.34	51.02	51.00	49.82
CaO			<0.04	0.15	<0.04	<0.04	<0.04	<0.04	<0.04	<0.04	0.17	<0.04	<0.04	<0.04	0.06	<0.04
Na_2O			<0.04	<0.04	<0.04	<0.04	<0.04	<0.04	<0.04	<0.04	<0.04	<0.04	<0.04	<0.04	<0.04	<0.04
NiO			0.47	0.28	0.41	0.46	0.44	0.42	0.40	0.39	0.39	0.44	0.44	0.43	0.45	0.45
Total			101.21	99.73	98.86	100.28	99.87	100.17	100.59	100.25	100.79	99.39	100.97	100.90	99.89	99.95
Mg#			0.940	0.916	0.921	0.917	0.918	0.917	0.909	0.907	0.913	0.916	0.917	0.917	0.922	0.905

Downloaded from https://academic.oup.com/petrology/article-abstract/doi/10.1093/petrology/egx062/4523818
by University of Durham user
on 07 November 2017

Spinel

	67-02A(1)	67-02B(6)	67-02B(2)	67-02D(3)	67-02A(2)	67-02B(1)	67-02D(1)	67-02D(4)	67-02E(1)	67-02A(3)	67-02A(5)	67-02B(3)	67-02B(5)	67-02D(7)	67-02E(3)
	P	P	D	D	H	H	H	H	H	H	H	H	H	H	H
SiO_2	<0.1	<0.1	<0.1	<0.1	<0.1	<0.1	<0.1	<0.1	<0.1	<0.1	<0.1	<0.1	<0.1	<0.1	<0.1
TiO_2	0.20	0.34	0.10	0.15	<0.05	<0.05	<0.05	<0.05	0.08	0.15	0.34	<0.05	0.37	0.08	<0.05
Al_2O_3	15.46	12.23	5.52	10.14	23.12	24.04	20.88	20.26	27.75	10.13	15.94	25.24	15.82	16.61	23.69
Cr_2O_3	49.44	53.80	63.19	51.74	44.76	43.27	43.82	48.08	40.53	54.31	51.19	45.73	50.17	50.91	43.92
Fe_2O_3	4.76	6.87	5.41	8.02	3.04	2.23	6.29	2.46	0.48	7.99	5.86	1.32	6.88	4.63	3.13
FeO	21.65	14.24	13.52	20.76	15.10	15.93	16.51	18.43	17.79	12.00	13.14	13.87	13.35	14.05	16.60
MnO	<0.12	<0.12	<0.12	<0.12	<0.12	<0.12	<0.12	<0.12	<0.12	<0.12	<0.12	<0.12	<0.12	<0.12	<0.12
MgO	8.07	12.75	12.46	7.76	13.09	12.46	11.78	10.87	12.24	13.42	13.91	14.54	13.72	13.12	12.21
CaO	<0.04	<0.04	<0.04	<0.04	<0.04	<0.04	<0.04	<0.04	<0.04	<0.04	<0.04	<0.04	<0.04	<0.04	<0.04
Na_2O	<0.04	<0.04	<0.04	<0.04	<0.04	<0.04	<0.04	<0.04	<0.04	<0.04	<0.04	<0.04	<0.04	<0.04	<0.04
NiO	0.10	0.11	0.09	0.06	0.09	0.07	0.13	0.06	0.09	0.16	0.16	0.07	0.16	0.16	0.10
Total	99.92	100.36	100.28	98.63	99.34	98.16	99.42	100.18	99.05	98.36	100.55	100.78	100.48	99.75	99.68
Mg#	0.40	0.61	0.62	0.40	0.61	0.58	0.56	0.51	0.55	0.67	0.65	0.65	0.65	0.62	0.57
Cr#	0.68	0.75	0.88	0.77	0.56	0.55	0.58	0.61	0.49	0.78	0.68	0.55	0.68	0.67	0.55
Fe2O3/FeO	0.22	0.48	0.40	0.39	0.20	0.14	0.38	0.13	0.03	0.67	0.45	0.10	0.52	0.33	0.19

Downloaded from https://academic.oup.com/petrology/article-abstract/doi/10.1093/petrology/egx062/4523818
by University of Durham user
on 07 November 2017

Orthopyroxene

	67-02A(1)	67-02B(6)	67-02B(2)	67-02D(3)	67-02A(2)	67-02B(1)	67-02D(1)	67-02D(4)	67-02E(1)	67-02A(3)	67-02A(5)	67-02B(3)	67-02B(5)	67-02D(7)	67-02E(3)
	P	P	D	D	H	H	H	H	H	H	H	H	H	H	H
SiO_2	55.97	57.48			56.98	55.60	56.53	57.20	57.26	57.29	56.00	56.53	56.91	56.48	55.82
TiO_2	<0.05	<0.05			<0.05	<0.05	<0.05	<0.05	<0.05	<0.05	<0.05	<0.05	<0.05	<0.05	<0.05
Al_2O_3	1.15	1.15			1.60	1.54	1.55	1.25	1.69	0.89	1.68	1.76	1.78	1.24	1.56
Cr_2O_3	0.48	0.46			0.53	0.47	0.59	0.45	0.46	0.40	0.57	0.61	0.49	0.49	0.44
FeO	7.17	5.75			5.26	5.44	5.45	5.99	5.70	5.35	5.53	5.60	5.62	5.13	6.17
MnO	0.16	0.15			0.14	0.13	0.13	0.14	0.13	0.15	0.14	0.15	0.10	0.13	0.16
MgO	34.86	35.10			34.99	35.58	34.96	35.21	34.90	35.04	35.17	35.52	35.41	35.43	34.83
CaO	0.59	0.81			0.89	0.51	1.12	0.60	0.53	1.23	0.48	0.40	0.56	0.60	0.67
Na_2O	<0.03	0.04			<0.03	<0.03	<0.03	<0.03	<0.03	<0.03	<0.03	<0.03	<0.03	<0.03	<0.03
NiO	0.09	0.08			0.07	0.10	0.09	0.08	0.09	0.12	0.10	0.09	0.10	0.08	0.07
Total	100.38	100.97			100.39	99.29	100.35	100.88	100.76	100.36	99.56	100.60	100.90	99.53	99.67
Mg#	0.897	0.916			0.922	0.921	0.920	0.913	0.916	0.921	0.919	0.919	0.918	0.925	0.910

Downloaded from https://academic.oup.com/petrology/article-abstract/doi/10.1093/petrology/egx062/4523818
by University of Durham user
on 07 November 2017

Clinopyroxene

	67-02A(1)	67-02B(6)	67-02B(2)	67-02D(3)	67-02A(2)	67-02B(1)	67-02D(1)	67-02D(4)	67-02E(1)	67-02A(3)	67-02A(5)	67-02B(3)	67-02B(5)	67-02D(7)		67-02E(3)
	P	P	D	D	H	H	H	H	H	H	H	H	H	H	H	H
SiO_2	54.38	53.50		52.68	53.22	53.54	53.39	53.29	54.34	54.82	52.57	53.81	52.68	53.04	51.94	53.44
TiO_2	0.08	0.11		0.05	<0.05	<0.05	<0.05	<0.05	0.06	<0.05	<0.05	<0.05	0.17	0.09	0.25	<0.05
Al_2O_3	1.26	1.25		0.48	1.66	1.29	1.40	1.26	1.39	0.55	1.37	1.15	2.41	2.01	2.71	1.61
Cr_2O_3	0.71	0.68		0.24	0.74	0.69	0.62	0.71	0.56	0.81	0.73	0.57	0.90	0.76	0.59	0.67
FeO	2.17	3.24		1.53	1.57	1.54	1.89	1.86	1.70	2.82	1.68	1.98	2.97	2.32	5.04	1.92
MnO	0.07	0.13		0.09	0.06	0.12	0.09	0.05	0.07	0.10	0.12	0.08	0.05	0.07	0.14	0.06
MgO	17.76	19.07		18.28	17.79	17.87	18.24	18.10	17.88	20.22	17.99	18.39	18.18	18.47	17.23	17.77
CaO	23.55	21.65		24.97	23.73	23.56	23.94	23.84	24.08	20.37	24.10	23.22	22.17	22.69	21.43	23.88
Na_2O	0.14	0.19		0.12	0.07	0.09	0.09	0.15	0.10	0.21	0.11	0.15	0.23	0.22	0.23	0.12
NiO	<0.05	0.05		<0.05	0.05	0.05	0.05	<0.05	0.05	0.06	0.05	0.02	0.07	0.07	0.03	0.06
Total	100.12	99.82		98.44	98.88	98.72	99.67	99.29	100.22	99.98	98.69	99.37	99.82	99.74	99.63	99.48
Mg#	0.936	0.913		0.955	0.953	0.954	0.945	0.945	0.949	0.927	0.950	0.943	0.916	0.934	0.859	0.943

Downloaded from https://academic.oup.com/petrology/article-abstract/doi/10.1093/petrology/egx062/4523818
by University of Durham user
on 07 November 2017

Table 3 Average major element composition of orthopyroxene and clinopyroxene from reaction patches from three samples. Mg# = Mg/Mg+Fe, Cr# = Cr/Cr+Al. Fe_2O_3 in spinel was calculated assuming ideal stoichiometry on a 3 cation basis

	67-02A(5) Cpx	67-02D(4) Cpx	67-02A(5) Opx	67-02B(3) Opx	67-02D(4) Opx 1	67-02D(4) Opx 2
SiO_2	54.88	54.48	57.71	57.62	58.47	57.97
TiO_2	0.09	0.07	<0.03	<0.03	<0.03	0.03
Al_2O_3	1.49	1.28	1.56	1.24	1.23	1.52
Cr_2O_3	0.37	0.66	0.42	0.19	0.82	0.42
FeO	4.00	3.60	5.34	4.91	2.47	5.26
MnO	0.13	0.13	0.14	0.12	0.02	0.13
MgO	20.21	20.61	34.39	36.16	37.43	35.98
CaO	18.38	18.74	0.76	0.46	0.17	0.69
Na_2O	0.10	0.13	<0.03	<0.03	0.04	<0.03
NiO	0.09	0.05	0.12	0.05	0.12	0.09
Total	99.74	99.75	100.46	100.76	100.77	102.11
Mg#	0.900	0.911	0.920	0.929	0.964	0.924

Downloaded from https://academic.oup.com/petrology/article-abstract/doi/10.1093/petrology/egx062/4523818
by University of Durham user
on 07 November 2017

Table 4 Average trace element concentrations of orthopyroxene. Values in italics are 1 s.d. on measurements from multiple crystals (number of crystals measured in parentheses). Also reported are typical detection limits and repeat measurements of natural standard glass BCR2G during the analytical sessions. Additional data for orthopyroxene and reaction patches can be found in the Supplementary Data.

	67-02A(1)	*1 s.d. (5)*	67-02B(6)	*1 s.d. (4)*	67-02A(2)	*1 s.d. (10)*	67-02B(1)	*1 s.d. (10)*	67-02D(1)	*1 s.d. (9)*	67-02D(4)	*1 s.d. (11)*	67-02E(1)	*1 s.d. (8)*
Na (ppm)					6.8	*3.8*	6.0	*3.0*	4.1	*2.2*	7.7	*2.5*	11.7	*10.7*
P (ppm)					22.6	*0.8*	20.2	*0.7*	21.9	*0.8*	20.4	*0.8*	13.1	*3.4*
Sc (ppm)	17.1	*2.6*			26.4	*1.3*	23.1	*1.0*	26.7	*2.2*	24.2	*2.0*	30.4	*0.9*
V (ppm)	45.0	*12.7*			43.1	*2.1*	47.3	*3.0*	57.8	*4.4*	42.3	*3.4*	61.0	*1.4*
Cr (ppm)					3089	*387*	3048	*501*	2954	*419*	2496	*366*	3124	*297*
Mn (ppm)					1026	*14*	1022	*17*	1102	*21*	1159	*23*	1036	*18*
Co (ppm)					50.6	*1.0*	52.7	*1.2*	52.4	*1.9*	52.7	*1.6*	52.5	*1.1*
Ni (ppm)					617	*28*	672	*35*	638	*42*	575	*27*	648	*23*
Ti (ppm)	144	*2.9*	50.3	*2.0*	10.7	*1.9*	6.8	*1.3*	27.0	*10.8*	29.5	*5.7*	82.7	*5.1*
Y (ppb)	158	*15.9*	147	*25.4*	33.2	*4.7*	48.6	*7.5*	96.8	*34.8*	101	*8.8*	187	*30.7*
Zr (ppb)	64.0	*11.2*	70.6	*4.7*	36.3	*5.7*	160	*23.5*	90.0	*23.9*	67.1	*11.6*	97.3	*15.9*
Nb (ppb)	3.7	*0.6*	1.4	*0.3*	6.2	*0.9*	7.9	*1.2*	6.2	*0.6*	6.5	*1.3*		
La (ppb)	1.0	*0.1*	0.49	*0.02*	0.31	*0.13*	0.78	*0.52*	0.54	*0.20*	0.23	*0.03*		
Ce (ppb)	3.4	*3.1*	1.9	*0.9*	0.67	*0.29*	2.5	*1.8*	1.3	*0.7*	0.53	*0.13*		
Pr (ppb)	0.53		0.36	*0.13*	0.22	*0.03*	0.58	*0.43*	0.46	*0.13*				
Nd (ppb)			4.2	*1.2*	1.7		3.6	*1.5*	3.3				4.5	
Sm (ppb)					0.80	*0.43*	2.0	*0.5*	1.4	*0.4*	0.91	*0.21*	3.1	*1.0*
Eu (ppb)	1.3	*0.1*	1.5	*0.1*			0.8	*0.3*	0.7	*0.1*	0.9			
Gd (ppb)	5.5	*0.8*	6.3	*0.6*	1.3	*0.6*	3.4	*1.2*	4.3	*1.0*	2.5	*0.2*	3.9	*0.9*
Tb (ppb)	1.3	*0.4*	1.3	*0.5*	0.3	*0.0*	0.60	*0.11*	1.0	*0.3*	0.80	*0.22*	1.5	*0.4*
Dy (ppb)	14.2	*1.4*	14.1	*2.0*	3.1	*0.8*	5.3	*1.1*	11.4	*3.5*	9.5	*1.9*	16.4	*4.5*
Ho (ppb)	5.3	*1.2*	4.8	*0.7*	1.1	*0.3*	1.6	*0.3*	3.5	*1.4*	3.6	*0.5*	6.1	*1.1*
Er (ppb)	23.4	*2.1*	20.6	*1.2*	5.8	*0.9*	7.0	*0.9*	16.0	*6.2*	15.7	*2.1*	31.7	*1.6*
Tm (ppb)	5.2	*1.4*	3.6	*0.4*	1.6	*0.3*	1.7	*0.4*	3.5	*1.1*	3.9	*0.5*	8.1	*1.3*
Yb (ppb)	50.8	*3.9*	38.1	*5.8*	23.7	*2.6*	20.7	*2.0*	39.1	*9.8*	39.6	*4.9*	78.4	*6.3*
Lu (ppb)	9.8	*0.5*	7.2	*1.1*	6.0	*0.7*	5.1	*0.6*	8.1	*1.9*	8.3	*1.2*	16.9	*3.7*
Hf (ppb)	3.7	*1.3*	2.4	*0.3*	1.0	*0.1*	3.2	*0.7*	3.5	*0.6*	2.0	*0.4*	2.6	*0.4*

Downloaded from https://academic.oup.com/petrology/article-abstract/doi/10.1093/petrology/egx062/4523818
by University of Durham user
on 07 November 2017

	67-02A(3)	*1 s.d. (9)*	67-02A(5)	*1 s.d. (8)*	67-02B(3)	*1 s.d. (10)*	67-02B(5)	*1 s.d. (4)*	67-02D(7)	*1 s.d. (11)*	67-02E(3)	*1 s.d. (4)*	L.O.D.	BCR2G	*1 s.d. (11)*
Na (ppm)	4.9	*1.4*	53.3	*31.4*	19.5	*36.5*	37.9	*15.2*	16.2	*9.7*	21.5	*14.6*	0.35	3.1	*0.1*
P (ppm)	20.6	*0.5*	22.5	*0.8*	7.9	*0.8*	9.5	*1.5*	20.5	*0.5*	21.3	*0.7*	0.75	1589	*28.58*
Sc (ppm)	25.5	*1.3*	23.4	*1.0*	26.8	*1.7*	25.2	*0.9*	24.5	*1.4*	26.3	*1.9*	0.01	33.30	*1.69*
V (ppm)	44.4	*1.8*	51.5	*2.1*	59.4	*2.7*	39.4	*2.3*	49.1	*2.8*	55.2	*3.3*	0.00	415	*7.75*
Cr (ppm)	2862	*315*	3679	*276*	3609	*570*	3313	*403*	2714	*212*	2648	*327*	0.12	14.61	*0.41*
Mn (ppm)	1044	*19*	1006	*14*	1011	*19*	978	*27*	1011	*19*	1135	*23*	0.09	1477	*33.4*
Co (ppm)	51.1	*1.0*	53.0	*0.8*	52.5	*1.5*	51.2	*0.7*	48.3	*0.9*	52.4	*1.8*	0.01	37.22	*0.84*
Ni (ppm)	619	*28*	668	*24*	683	*43*	645	*22*	580	*27*	624	*46*	0.12	13.9	*3.75*
Ti (ppm)	10.7	*0.4*	33.8	*3.8*	23.3	*1.2*	13.1	*1.7*	44.4	*4.6*	18.1	*2.6*	0.05	12783	*238*
Y (ppb)	29.7	*2.7*	79.5	*10.4*	32.1	*7.0*	25.9	*4.6*	124	*58.2*	101	*17.0*	1.75	31.05	*1.43*
Zr (ppb)	37.6	*2.0*	93.9	*9.5*	16.7	*4.7*	58.8	*7.4*	201	*82.8*	73.1	*16.5*	2.21	174	*7.47*
Nb (ppb)	7.5	*0.8*	9.3	*1.0*					5.3	*0.8*	6.9	*0.7*	0.42	11.76	*0.25*
La (ppb)	0.46	*0.56*	2.20	*1.57*	2.71		5.18	*2.72*	0.54	*0.21*	0.67		0.20	24.4	*1.01*
Ce (ppb)	0.94	*0.66*	4.78	*2.84*	1.56	*0.66*	11.40	*5.76*	1.95	*0.66*	0.79	*0.73*	0.15	50.8	*0.88*
Pr (ppb)	0.30	*0.28*	0.76	*0.36*	0.88		1.44	*0.73*	0.47	*0.12*	0.32		0.14	6.53	*0.17*
Nd (ppb)	3.7	*2.3*	4.1	*0.4*	3.8		6.4	*4.5*	4.4	*2.0*			1.38	27.8	*0.92*
Sm (ppb)	0.87	*0.76*	1.54	*0.82*	2.20	*0.50*	2.75	*1.66*	2.41	*1.66*	1.73	*0.31*	1.36	6.54	*0.30*
Eu (ppb)									1.99	*0.43*	0.95	*0.14*	0.42	1.94	*0.06*
Gd (ppb)	2.0	*0.3*	2.5	*0.8*			3.4	*0.4*	5.3	*3.0*	6.1	*0.4*	1.14	6.45	*0.29*
Tb (ppb)	0.37	*0.04*	0.52	*0.22*	0.42	*0.09*	0.57	*0.18*	1.39	*0.69*	0.92	*0.25*	0.25	0.93	*0.01*
Dy (ppb)	2.6	*0.5*	7.6	*1.6*	2.9	*0.8*	3.3	*1.3*	14.4	*8.5*	11.4	*2.6*	0.94	6.13	*0.23*
Ho (ppb)	1.0	*0.1*	2.5	*0.4*	0.88	*0.31*	0.89	*0.36*	4.1	*2.1*	3.3	*0.7*	0.27	1.16	*0.02*
Er (ppb)	5.2	*0.5*	12.3	*1.8*	6.8	*1.5*	4.9	*0.7*	18.2	*7.1*	13.2	*1.2*	1.35	3.51	*0.17*
Tm (ppb)	1.7	*0.3*	2.9	*0.2*	2.1	*0.6*	2.1	*0.2*	4.2	*1.1*	3.0	*0.4*	0.58	0.47	*0.01*
Yb (ppb)	22.4	*2.6*	34.7	*2.6*	30.5	*5.9*	28.4	*2.1*	41.1	*8.2*	36.1	*2.3*	1.35	3.17	*0.14*
Lu (ppb)	6.0	*0.2*	7.9	*1.0*	7.6	*1.2*	7.7	*0.3*	9.1	*1.6*	7.7	*0.7*	0.38	0.46	*0.03*
Hf (ppb)	1.1	*0.1*	2.1	*0.3*	1.1		1.1		7.3	*3.5*	1.3	*0.3*	0.80	4.57	*0.11*

Downloaded from https://academic.oup.com/petrology/article-abstract/doi/10.1093/petrology/egx062/4523818
by University of Durham user
on 07 November 2017

Table 5 Average trace element concentrations of clinopyroxene. Values in italics are 1 s.d. on measurements from multiple crystals (number of crystals measured in parentheses)

	67-02A(1)	*1 s.d. (2)*	67-02B(6)	*1 s.d. (4)*	67-02A(2)	*1 s.d. (11)*	67-02B(1)	*1 s.d. (5)*	67-02D(1)	67-02D(4)	*1 s.d. (5)*	67-02E(1)	*1 s.d. (7)*	67-02D(7)	*1 s.d. (5)*
P (ppm)			22.5	*1.9*	20.0	*1.9*	20.8	*1.9*	22.8	21.6	*2.12*	22.4	*1.8*	22.4	*2.3*
Sc (ppm)	64.1	*3.4*	56.5	*8.9*	54.5	*1.8*	60.5	*3.3*	62.9	63.7	*5.33*	93.9	*11.4*	106	*21*
Ti (ppm)	312	*10*	303	*171*	17.2	*3.6*	15.6	*3.0*	68	49.4	*10.8*	289	*60*	1504	*199*
V (ppm)	154	*3*	143	*64*	76.3	*7.2*	94.0	*10.9*	127	88.6	*16.8*	187	*38*	346	*44*
Cr (ppm)			4451	*954*	4212	*662*	4583	*250*	4604	4302	*693*	3917	*1567*	2709	*1518*
Ni (ppm)			353	*28*	319	*18*	348	*27*	340	310	*22.1*	349	*15*	352	*96*
Sr (ppm)			12.4	*5.5*	5.39	*1.0*	15.6	*5.2*	15.9	5.82	*1.64*	11.6	*1.5*	31.3	*0.8*
Y (ppb)	2019	*92*	2646	*1159*	315	*45*	456	*101*	1736	1066	*324*	2436	*493*	7679	*1236*
Zr (ppb)	1149	*34*	1539	*398*	321	*58*	1484	*310*	1489	728	*223*	1541	*439*	2199	*366*
Nb (ppb)	5.4	*0.9*	6.8	*0.97*	6.6	*1.6*	6.6	*0.7*	5.1	6.7	*1.5*	6.9	*2.8*	4.8	*2.4*
La (ppb)	57.7	*1.4*	116	*29*	47.9	*19.0*	160	*78*	167	28.7	*10.4*	94.7	*21.7*	196	*19*
Ce (ppb)	251	*9*	416	*106*	175	*66*	616	*314*	575	113	*46*	382	*89*	1010	*82*
Pr (ppb)	56.2	*0.7*	83.2	*24.3*	35.6	*13.9*	116	*55*	111	28.2	*11.8*	79.5	*16.4*	264	*28*
Nd (ppb)	381	*35*	509	*149*	200	*72*	599	*301*	725	186	*87*	528	*123*	1985	*267*
Sm (ppb)	177	*13*	204	*78*	66.3	*22.9*	166	*59*	268	98.0	*37.4*	244	*58*	914	*173*
Eu (ppb)	66.4	*0.9*	84.6	*23.4*	21.7	*6.4*	50.7	*19.8*	91.7	34.3	*11.2*	75.7	*17.3*	336	*53*
Gd (ppb)	291	*30*	357	*154*	66.4	*17.0*	142	*53*	339	141	*54*	342	*81*	1327	*202*
Tb (ppb)	47.4	*2.4*	64.3	*26.3*	8.9	*1.9*	17.0	*4.4*	51.9	25.1	*8.0*	60.3	*14.0*	224	*37*
Dy (ppb)	372	*14*	485	*236*	54.2	*10.4*	97.4	*37.4*	342	195	*63*	421	*86*	1558	*260*
Ho (ppb)	77.5	*8.6*	103	*49*	11.8	*2.0*	19.4	*5.9*	72.1	42.3	*11.4*	98.0	*20.5*	318	*51.9*
Er (ppb)	248	*30*	308	*138*	45.4	*8.4*	56.6	*19.2*	187	128	*33*	314	*62*	915	*154*
Tm (ppb)	31.6	*3.4*	43.9	*20.7*	8.7	*2.3*	10.8	*3.0*	30.1	19.9	*5.5*	46.6	*8.6*	116	*17.7*
Yb (ppb)	224	*6*	271.5	*136*	80.4	*11.5*	82.8	*16.3*	192	144	*35*	323	*62*	771	*136*
Lu (ppb)	31.5	*2.7*	38.6	*16.9*	15.5	*2.2*	15.8	*4.7*	27.8	22.4	*5.6*	50.4	*9.6*	102	*20.4*
Hf (ppb)	53.3	*6.5*	56.6	*22.3*	9.1	*1.9*	41.5	*25.1*	74.0	29.0	*10.9*	80.4	*25.4*	149	*26.4*

Downloaded from https://academic.oup.com/petrology/article-abstract/doi/10.1093/petrology/egx062/4523818
by University of Durham user
on 07 November 2017

Table 6 Trace element composition of olivine (ppm). Data are displayed as maximum compositional diversity observed in each sample from many crystal measurements (number of crystals italicised and in parentheses). Representative limit of detection (L.O.D.) also reported.

	67-02B(2)	67-02D(3)	67-02A(2)	67-02B(1)	67-02D(1)	67-02D(4)	67-02E(1)	67-02A(3)	67-02A(5)	67-02B(5)	67-02D(7)	67-02E(3)	
n=	*10*	*23*	*42*	*39*	*25*	*39*	*35*	*23*	*25*	*35*	*37*	*20*	*L.O.D.*
Na	0.75-6.18	<0.47	<0.31	<0.36 - 2.48	<0.36	<0.26	<0.28	1.44 - 22.8	<0.35 - 11.6	<0.28 - 9.61	<0.37 - 7.9	<0.17 - 2.20	0.35
Al	0.82-21	0.59 - 6.00	3.02 - 5.08	2.56 - 9.82	2.59 - 9.05	1.06 - 3.34	1.75 - 5.55	22.2 - 41.6	4.2 - 56.8	13.0 - 49.9	15.1 - 36.6	2.5 - 7.1	0.04
P	19-22	19 - 22	17 - 19	15 - 18	16 - 19	17 - 19	17 - 20	15 - 18	17 - 22	16 - 26	16 - 18	16 - 18	0.39
Ca	21-120	45- 131	41 - 90	32 - 96	39 - 140	33 - 88	26 - 104	77 - 793	29 - 166	46 - 599	22 - 302	28 - 95	1.9
Sc	3.06-4.14	3.50 - 4.29	3.26 - 3.80	3.06 - 3.40	2.90 - 3.57	3.15 - 3.50	3.26 - 3.82	3.13 - 5.30	2.77 - 3.62	3.63 - 6.57	2.83 - 4.30	2.58 - 3.15	0.004
Ti	1.89-2.93	2.28 - 4.16	0.99 - 1.28	0.88 - 1.62	1.19 - 2.01	1.28 - 2.36	2.40 - 4.04	0.75 - 5.74	1.07 - 2.96	1.21 - 10.5	1.54 - 5.55	0.80 - 1.47	0.02
V	0.02-0.34	0.08 - 0.54	0.28 - 0.42	0.27 - 0.58	0.31 - 1.02	0.23 - 0.42	0.35 - 0.63	1.82 - 3.19	0.32 - 2.43	0.39 - 3.83	0.54 - 3.00	0.31 - 0.42	0.002
Cr	5.9-13.1	3.84 - 13.8	4.0 - 10.4	4.4 - 28.6	5.5 - 18.6	4.92- 9.0	5.5 - 13.2	16 - 265	5 - 119	7 - 147	7.2 - 54.2	5.1 - 13.7	0.06
Mn	597-718	949 - 979	935 - 981	929 - 1013	975 - 1023	1022 - 1071	969 - 1028	955 - 1163	939 - 993	919 - 1289	910 - 1166	1035 - 1078	0.04
Co	89-115	126 - 135	135 - 143	140 - 148	138 -144	137 - 145	138 - 143	135 - 142	134 - 143	137 - 141	131 - 137	144 - 149	0.004
Ni	3121-3270	2740 - 2877	3079 - 3237	3166 - 3439	3112 - 3231	2835 - 2996	2971 - 3154	2792 - 3181	3013 - 3221	2753 - 3205	2875 - 3017	3069 - 3204	0.08
Y (ppb)	0.58-7.54	<0.12 - 2.10	<0.23 - 1.00	<0.26 - 3.7	<0.26 - 0.59	<0.23 - 0.82	<0.23 - 2.18	1.07 - 20.9	<0.27 - 13.7	<0.23 - 23.8	<0.25 - 20.7	<0.11 - 0.53	0.22

Downloaded from https://academic.oup.com/petrology/article-abstract/doi/10.1093/petrology/egx062/4523818
by University of Durham user
on 07 November 2017

Table 7 Temperatures (°C) calculated from average mineral compositions and summary of relevant mineral compositional data for comparison. Temperatures in brackets were calculated using fine-grained pyroxenes within reaction patches. 'ONW' is the olivine-spinel thermometery of O'Neill & Wall (1987), 'WCC' is the olivine-spinel Al exchange thermometer of Wan *et al.* (2008), 'DHGC' is the Al in olivine thermometer of De Hoog *et al.* 2010, 'BKN' is the two-pyroxene and Ca-in-orthopyroxene thermometers of Brey & Köhler (1990) and 'LSY' is the 2-pyroxene REE exchange thermometer of Liang *et al.* (2013). Variation in temperature calculated from different mineral pairs in each sample is similar to the assumed uncertainty in the thermometry calibrations of ± 50 °C. A pressure of 1.5 GPa was assumed in all calculations. Mg# = Mg/Mg+Fe, Cr# = Cr/Cr+Al. Italicised samples are those for which all thermometry calculations could be performed, and the discussion on sub-solidus cooling refers to these samples solely. Sample 67-02D(4) displays reaction textures in the thin section, but not in the thick section. The two bracketed values for the thin section were calculated from populations 1 and 2 of secondary opx.

Sample	Lithology	*Reaction* textures?	T (ONW)	T (WCC)	T (DHGC)	T (BKN; 2 pyx)	T (BKN; Ca opx)	T (LSY)	Olivine Mg#	Spinel Cr#
67-02A(1)	Pyroxenite					880	930	970		0.68
67-02B(6)	Pyroxenite					1070	1000	930		0.75
67-02B(2)	Dunite		910						0.940	0.88
67-02D(3)	Dunite		680						0.921	0.77
67-02A(2)	*Harzburgite*	*No*	*760*	*690*	*650*	*840*	*910*	*1000*	*0.917*	*0.56*
67-02B(1)	*Harzburgite*	*No*	*700*	*700*	*650*	*860*	*900*	*980*	*0.918*	*0.55*
67-02D(1)	*Harzburgite*	*No*	*730*	*740*	*660*	*820*	*900*	*820*	*0.917*	*0.58*
67-02D(4)	*Harzburgite*	*No (thick section)*	*700*	*650*	*620*	*790*	*890*	*990*	*0.909*	*0.61*
67-02E(1)	*Harzburgite*	*No*	*660*	*670*	*650*	*820*	*900*	*950*	*0.907*	*0.49*
67-02A(3)	Harzburgite	Yes	1130	1010	870	1170	1110		0.913	0.78
67-02A(5)	Harzburgite	Yes	980	870	740	710 (1260)	890 (980)		0.916	0.68
67-02B(3)	Harzburgite	Yes	810			910	850 (860)		0.917	0.55
67-02B(5)	Harzburgite	Yes	960	940	790	1020	920		0.917	0.68
67-02D(4)	Harzburgite	Yes (thin section)				(1260, 1220)	(760, 960)			
67-02D(7)	Harzburgite	Yes	870	880	760	970	930	670	0.922	0.67
67-02E(3)	Harzburgite	Yes	750	690	650	810	960		0.905	0.55

Downloaded from https://academic.oup.com/petrology/article-abstract/doi/10.1093/petrology/egx062/4523818
by University of Durham user
on 07 November 2017

Downloaded from https://academic.oup.com/petrology/article-abstract/doi/10.1093/petrology/egx062/4523818
by University of Durham user
on 07 November 2017

Appendix Table Compilation of values used for the melting models. See the *Discussion* for a detailed description of the model used and data sources

	Hydrous	Anhydrous
Starting material	High MgO basalt	Refractory lherzolite
T (°C)	1245	1315
P (Gpa)	1.3	1.5
Partition coefficients		
Y (cpx)	0.561	0.76
Yb (cpx)	0.543	0.76
Y (opx)	0.101	0.086
Yb (opx)	0.164	0.168
Initial modes		
Cpx	0.18	0.18
Opx	0.25	0.25
Ol	0.55	0.55
Sp	0.02	0.02
Lherzolite melting reactions		
Cpx	0.62	0.71
Opx	0.51	0.38
Ol	-0.25	-0.22
Sp	0.12	0.13
Harzburgite melting reaction		
Opx	0.87	
Ol	0.23	

Downloaded from https://academic.oup.com/petrology/article-abstract/doi/10.1093/petrology/egx062/4523818
by University of Durham user
on 07 November 2017